Impacts of Natural and Anthropogenic Aerosols on Atlantic Tropical Cyclones

A Dissertation

by

BOWEN PAN

Submitted to the Office of Graduate and Professional Studies of
Texas A&M University
in partial fulfillment of the requirements for the degree of

DOCTOR OF PHILOSOPHY

Chair of Committee,	Renyi Zhang
Committee Members,	William K. Lau
	Robert L. Korty
	Qi Ying
Head of Department,	R. Saravanan

December 2019

Major Subject: Atmospheric Sciences

ABSTRACT

This dissertation investigated the impacts of natural and anthropogenic aerosols on Atlantic tropical cyclones by combining observational analyses and numerical modeling. The objectives of the research were to assess the impacts of anthropogenic aerosols on Hurricane Harvey (2017) and Saharan dust on two hurricanes, Danielle and Earl (2010).

Hurricane Harvey made landfall near Rockport, Texas, as a category 4 hurricane on 26 August. Harvey produced heavy rainfall of about 555 mm in the Houston urban area during 25-27 August. Ground- and satellite-based lightning and ground-based radar reflectivity measurements were analyzed, showing unusually intense lightning (over 0.23 million strikes) and radar reflectivity in the Houston region during 26-27 August. The effects of anthropogenic aerosols on precipitation and lightning during Harvey was investigated using a Cloud-Resolving Weather and Research Forecasting (CR-WRF) model. The ensemble simulations spanned from 25 to 28 August. The simulations show that anthropogenic aerosols increase precipitation and lightning in Houston by a factor of 2-3, unraveling the dominant factor of regulating the energetics and flooding during this extreme weather event. Combined measurements and numerical model simulations were made to show fundamentally altered cloud microphysical and thermodynamic processes of Hurricane Harvey by anthropogenic aerosols.

The second part of this dissertation evaluated the impacts of Saharan dust during Hurricanes Danielle and Earl (2010). Hurricanes Danielle and Earl both originated from the West African coast and developed under similar large-scale dynamic conditions and

coexisted in the different stages of their life cycles and were subjected to the intrusion of Saharan dust. The CR-WRF was used in conjunction with an aerosol-aware two-moment bulk microphysics scheme, accounting for dust as ice nucleating particles (INPs) and dust radiative forcing. The model simulations reveal that the radiative effect of dust significantly decreases or increases temperature or moisture below 600 mb. The change in the temperature field perturbs the large-scale circulation and alters the tracks of Hurricanes Danielle and Earl. In addition, the dust radiative effect significantly decreases the intensity of Hurricane Earl due to increased vertical wind shear and decreased surface sensible and latent heat fluxes. Dust serving as INPs enhances the formation of ice hydrometeors, but plays an insignificant role in the intensity of both hurricanes.

DEDICATION

This dissertation is dedicated to my grandfather who passed away during the course of my graduate school and to my parents for their tremendous support and unconditional love.

ACKNOWLEDGEMENTS

First, I want to acknowledge my advisor Dr. Renyi Zhang for his support throughout my graduate school. His dedication and passion in research ignited my passion to pursue a higher degree and a career in science. In addition, I deeply appreciate the help and support from my committee advisors, Drs. William K. Lau, Robert L. Korty, and Ying Qi throughout the course of this research.

Thanks also go to Dr. Yuan Wang from the California Institute of Technology who provided many valuable inputs on this dissertation research. I want to express my appreciation to Drs. Jiaxi Hu and Yun Lin for their tremendous help on modeling and research. Moreover, I want to thank Dr. Jenshan Shieh for his suggestions on analyses on this research. Thanks also go to Drs. Tim Logan and Richard Weitz for their tremendous help on the lightning data analyses. I want to thank Yixin Li for his help on the microphysics analyses. I also appreciate Claire Onak who helped process the lightning data. Special thanks to Dr. Jiwen Fan from the Pacific Northwest National Laboratory for her suggestion on the model configuration.

Thanks to my parents for their encouragement, patience and unconditional love. Thanks also go to my fiancé, Dr. Jake Mulholland, who always supported me throughout my Ph.D. journey. I forever grateful for group members from Dr. Renyi Zhang's group. They have made Texas A&M University a second home. I deeply appreciated friends, colleagues, and the department faculties and staff members for making my time at Texas A&M University a great experience.

Many thanks to the supercomputer facility of Texas A&M University, especially Ping Luo, who helped me set up the regional climate models on their facility.

CONTRIBUTORS AND FUNDING SOURCES

Contributors

Contributors This work was supported by a dissertation committee consisting of Professor Renyi Zhang and Robert L. Korty and William K. Lau of the Department of Atmospheric Sciences and Professor Qi Ying of the Department of Civil Engineering.

The Houston Lightning Mapping Array data for Chapter II was provided by Professor Timothy Logan of the Department of Atmospheric Sciences. The Köhler Curve depicted in Chapter II was provided by Yixin Li of the Department of Chemistry. The lightning strike analyses in Chapter II was provided by an Research Education Undergraduate student, Claire Onak. The initial condition of the model simulations in Chapter II was provided by Dr. Yuan Wang from California Institute of Technology.

All other work conducted for the dissertation was completed by the student independently.

Funding Sources

This doctoral research was supported by a NASA Earth and Space Science Fellowship.

NOMENCLATURE

ACI	Aerosol-Cloud Interaction
AEJ	African Easterly Jet
AEW	African Easterly Waves
AOD	Aerosol Optical Depth
ARI	Aerosol-Radiative Interaction
CAM	Community Atmospheric Model
CAPE	Convective Available Potential Energy
CCN	Cloud Condensation Nuclei
CFADs	Contoured-frequency-by-altitude diagrams
CFSR	Climate Forecast System Reanalysis
CIN	Convective Inhibition
CR-WRF	Cloud Resolving Weather Research and Forecasting Model
DMS	Dimethylsulfide
ERF	Effective radiative forcing
GLM	Geostationary Lightning Mapper
GOES-16	Geostationary Operational Environmental Satellite system
HLMA	Houston Lightning Mapping Array
INP	Ice Nucleating Particle
IPCC	Intergovernmental Panel on Climate Change
ITCZ	Intertropical Convergence Zone

IWP	Ice Water Path
LPI	Lightning Potential Index
LWP	Liquid Water Path
MCS	mesoscale convective systems
MODIS	Moderate Resolution Imaging Spectroradiometer
MPE	Multisensor Precipitation Estimates
MSLP	Mean Sea-Level Pressure
NEXRAD	Next Generation Radar
NLDN	National Lightning Detection Network
OPAC	Optical Properties of Aerosols and Clouds
PI	Potential Intensity
$PM_{2.5}$	particulate matter smaller than 2.5 μm
QPF	quantitative precipitation forecast
RAMS	Regional Atmospheric Model System
RFCs	River Forecast Centers
RF	Radiative forcing
RH	Relative Humidity
SAL	Saharan Air Layer
SSA	Sea Spray Aerosol
SST	Sea Surface Temperature
TAMU	Texas A&M University
TC	Tropical Cyclone

UAP	Ultrafine Aerosol Particles
VHF	Very High Frequency
WSR-88D	the Weather Surveillance Radar, 1988, Doppler

TABLE OF CONTENTS

Page

LIST OF FIGURES

Page

LIST OF TABLES

Page

1. INTRODUCTION

Atmospheric aerosols, which are defined as liquid or solid particles suspended in air, have profound impacts on weather and climate as well as other broad societal implications (IPCC 2013). For example, aerosol particles absorb and scatter incoming solar radiation in the atmosphere, which is commonly referred to as the aerosol radiation interaction (ARI), and significantly impacts the Earth energy budget. The ARI effect contributes to cooling (by scattering and absorption) and warming (by absorption) in the atmosphere (IPCC 2013; Peng et al. 2016; Wang et al. 2013) and alters the vertical temperature profile and atmospheric stability. This ARI effect also influences convection initiation and development as well as sea surface temperature (SST). By acting as CCN and ice nucleating particles (INPs), aerosols also play an important role in the cloud formation/development, precipitation efficiency, albedo, frequency, and lifetime of clouds. This later effect is commonly referred to as the aerosol cloud interaction (ACI) (Fan et al. 2018; Li et al. 2008; Rosenfeld et al. 2008), which is also critical to the radiative budget in the atmosphere. Presently, the aerosol effects associated with ARI and ACI represent the largest uncertainty in predictions of anthropogenic forcing on climate (Figure 1) (IPCC 2013).

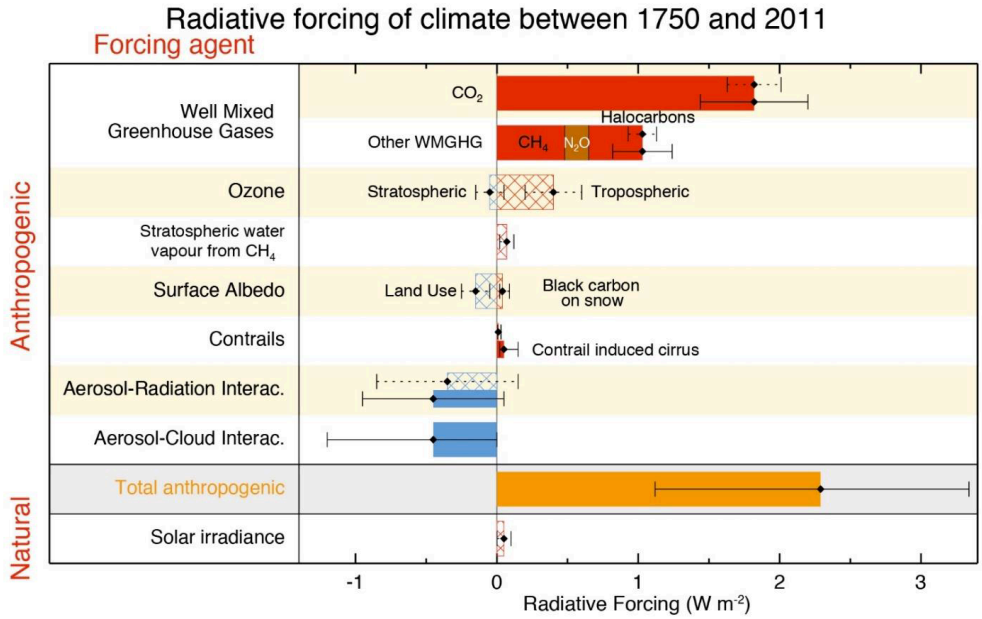

Figure 1: Radiative forcing (RF) and Effective radiative forcing (ERF) of climate change during the Industrial Era. Bar chart for Radiative Forcing (RF, hatched) and Effective Radiative Forcing (ERF, solid) for the period 1750–2011. Uncertainties (5 to 95% confidence range) are given for RF (dotted lines) and ERF (solid lines) (IPCC 2013).

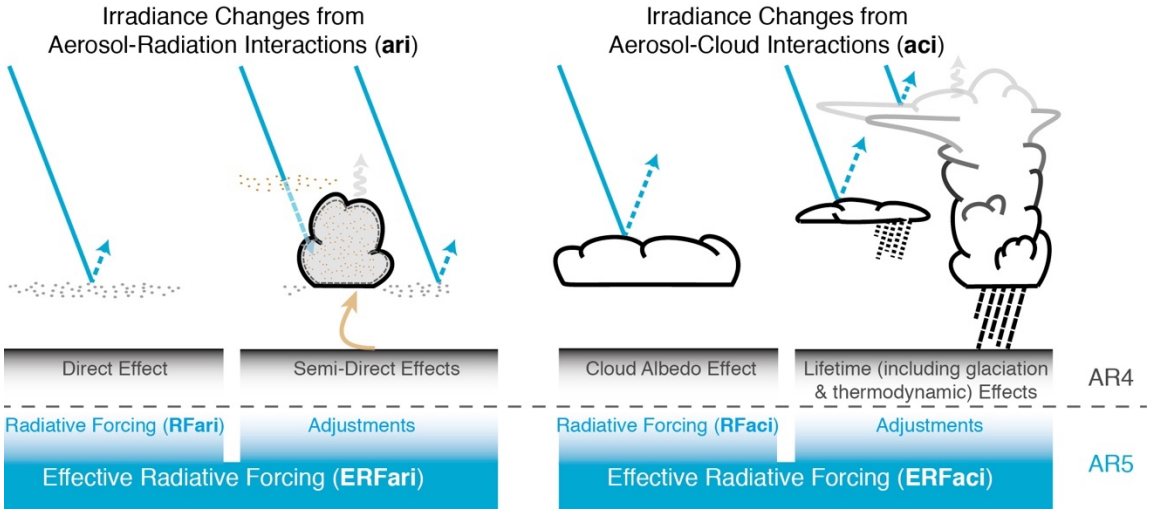

Figure 2: Schematic of aerosol–radiation and aerosol–cloud interactions in the Assessment Report (AR4) and AR5. The blue arrows depict solar radiation, the grey arrows terrestrial radiation and the brown arrow symbolizes the importance of couplings between the surface and the cloud layer for rapid adjustments (IPCC 2013).

As shown in Figure 2, the concept of ACI was traditionally established on the basis of the Twomey effect. Twomey (1974) first proposed that activation of more numerous aerosols leads to smaller cloud droplets and higher cloud albedo, also known as the cloud albedo effect. In addition, Albrecht (1989) indicated that a higher aerosol concentration leads to a longer cloud lifetime, as known as the cloud lifetime effect. Moreover, absorbing aerosols, such as black carbon, warm the mid-level atmosphere, modify the atmospheric lapse rate, and possibly decrease the cloud fraction and suppress convective activities (Hansen et al. 1997), which is also known as the aerosol semi-direct effect. The subject on ACI and ARI has advanced significantly over the last decade, particularly in terms of cloud invigoration and precipitation enhancement by anthropogenic aerosols (Rosenfeld et al. 2008; Li et al., 20108; Wang et al., 2013). Cloud invigoration occurs via microphysical and thermodynamics processes, which are associated with the ACI and ARI, respectively. For example, elevated aerosol levels modify warm and mix-phase microphysical processes (Figure 3, Rosenfeld et al. 2008), which impacts cloud formation (lifetime, vertical and horizontal extends, and properties of hydrometeors), albedo, precipitation efficiency, and cloud electrification (e.g., (Rosenfeld et al. 2008). Recently, several studies have suggested alternative cloud invigoration pathways by aerosols. For example, Fan et al. (2013) showed that the conventional concept of aerosol invigoration contributes limitedly to the observed increases of cloud top height and cloud cover. Their work revealed a dominant mechanism for aerosol invigoration via the microphysics effect, by extending the cloud top height and producing a large cloud cover that are critical to the Earth radiative budget. In addition, Fan et al. (2015) revealed a substantial effect of air

pollution to catastrophic floods by establishing a mechanism of aerosol-enhanced conditional instability. Most recently, Fan et al. (2018) discovered a mechanism of ultrafine aerosol particles (UAPs) in drastically invigorating convective intensity and enhancing precipitation by combined field observations and process-level modeling. Previously, UAP are thought to be too small to activate as cloud condensation nuclei under atmospheric conditions. Because UAPs exist in exceedingly high concentrations in present days, this work has profound implications on weather and climate. The cloud invigoration mechanism via thermodynamic processes is relevant to inhibited low-level convection, but enhanced upper-level convective available potential energy (CAPE) by light-absorbing aerosols (Wang et al. 2013, Figure 4). Both microphysical and thermodynamic aerosol invigorations of deep convective clouds have now been well recognized for their profound impacts on cloud formation, precipitation, hydrological cycle, and climate.

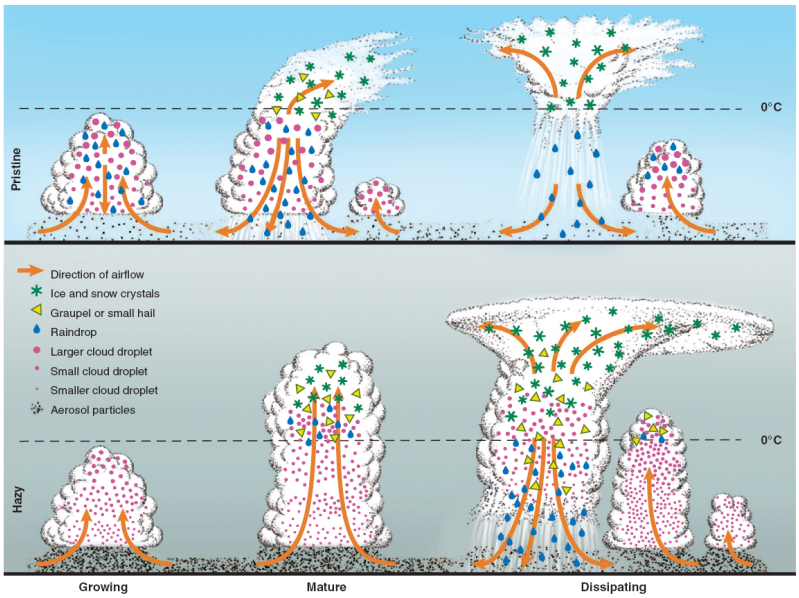

Figure 3: Evolution of deep convective clouds developing in the pristine (top) and polluted (bottom) atmosphere from (Rosenfeld et al. 2008).

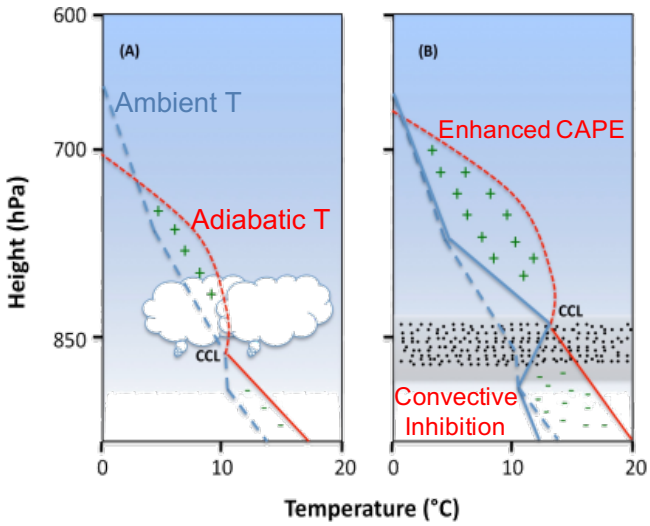

Figure 4: Schematic depiction of the atmospheric effects of light absorbing aerosols on convection and cloud formation: (A) without and (B) with the presence of absorbing aerosols in the Planetary Boundary Layer (PBL) (Wang et al. 2013).

Tropical Cyclones (TCs) are one of the most destructive weather phenomena and have exerted significant economic and societal impacts on human society. TCs are categorized according to its 1-min maximum sustained wind speed and minimum pressure into: tropical depression ($\leq$ 17 m/s), tropical storm (18-32 m/s), and severe tropical cyclone ($\geq$ 33 m/s) according to the Saffir-Simpson hurricane wind scale. The genesis and development of TCs are regulated by the Coriolis force and various environmental conditions, including SST, vertical wind shear, relative vorticity, and atmospheric stability (Gray 1998). For example, a SST of warmer than 26.5ºC, high relative vorticity, high moisture content, and low vertical wind shear are favorable for TC genesis and development. In addition, over the Atlantic Ocean, nearly half of the TCs are formed associated with the African Easterly Waves (AEWs) where the environment obtains sufficient moisture and high relative vorticity.

The genesis and development of TCs are also linked to aerosols, because aerosols directly perturb the atmospheric temperature profile (via ARI) and indirectly affect the cloud microphysical processes (via ACI). The aerosol impacts on TCs have been an active research topic since the Project Stormfury from 1962 to 1983 (Willoughby et al. 1985). The ACI effect on TCs depends on the spatial distribution and chemical composition of aerosols and the lifecycle of TCs. For example, increasing CCN concentrations at the tropical cyclone periphery can lead to weakening of TC intensity (Carrio and Cotton 2011; Hazra et al. 2013; Krall and Cottom 2012; Lynn et al. 2016; Rosenfeld et al. 2012; Wang et al. 2014; Zhang et al. 2007; Zhang et al. 2009). Also, Rosenfeld et al. (2012) have shown that aerosols invigorate convection and strengthen the downdraft, by cutting off the air spirals into the center of TCs and weakening the TC development. Wang et al. (2014) have also illustrated that anthropogenic aerosols profoundly impact TCs; the coupled microphysical and radiative effects of anthropogenic aerosols result in delayed development, weakened intensity, and early dissipation of TCs, but an enlarged rainband and increased precipitation under polluted conditions (Figure 5). Those previous studies showed that aerosols invigorate the convection activities near the rainband region, increases the cold pool intensity, and impedes the warm and moist air inflow to the TC eyewall, therefore decreasing the TC intensity. On the other hand, an increase of CCN near the TC eyewall can lead to intensification of TCs (Herbener et al. 2014; Khain et al. 2016). Aerosols invigorate the eyewall convection, increases the pressure gradient between eyewall and rainband, and further increases the TC intensity. In addition, Herbener et al. (2014) indicated the possibility of coexistence of invigorations in both

regions, resulting in a non-linear response of TC intensity to aerosol concentration. Qu et al. (2017) recently assessed the convection competition between the eyewall and rainbands due to ACI effect and found an increased minimum pressure in TC Saomai (2006). In addition, another recent observational analysis has shown enlarged rainfall areas of tropical cyclones over the western North Pacific by anthropogenic aerosols (Zhao et al. 2018).

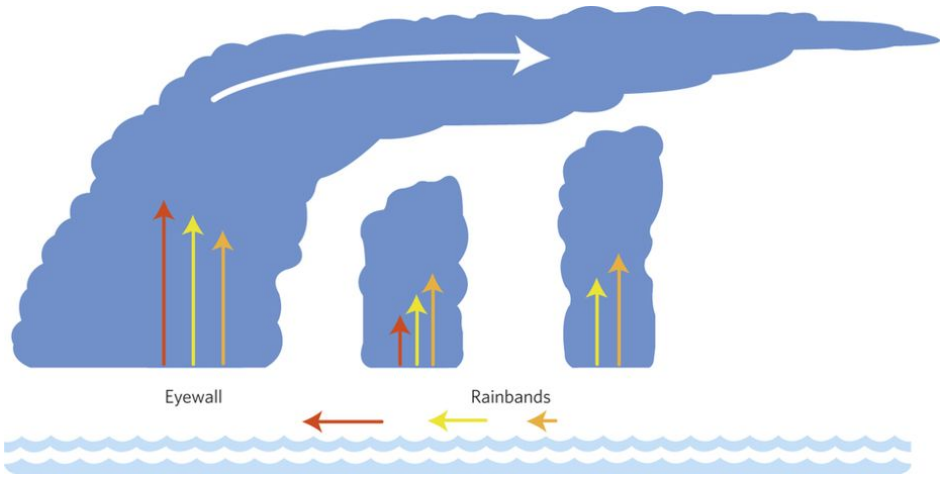

Figure 5: Schematic of the microphysical and radiative effects of anthropogenic aerosols on TCs. The development of TCs is characterized by the vertical velocities in the peripheral rainband and eyewall regions (vertical arrows) and the lower-level inflow (horizontal arrows). The red, yellow, and orange arrows represent the clean, polluted, and polluted with aerosol radiative effects, respectively.

The ACI and ARI effects on TCs are sensitive to the aerosol species. Marine aerosols are either emitted directly into the atmosphere (primary) or produced from new particle formation via gas-to-particle conversion (secondary) in the atmosphere. A wide variety of aerosol types, which originate from new particle formation, primary production from sea-spray, ship emissions, and long-range transport of natural and anthropogenic particles from the continents, exist in marine environments. For example, the oxidation

products of dimethylsulfide (DMS), iodine compounds, and amines are believed to be the important biogenic precursors for new particle formation (e.g., Charlson et al. 1987; O'Dowd and de Leeuw, 2007; Quinn and Bates, 2011; Zhang et al. 2012; Qiu and Zhang, 2013; Sellegri et al. 2016). Furthermore, it is plausible that photochemical oxidation products of volatile organic compounds, which enter the atmosphere via air-sea exchange, play a role in nucleation and growth of nanoparticles (Zhang et al. 2010; Zhao et al. 2009; Xu and Zhang 2013). In addition to sea-salt, organic matter may also be transferred to the atmosphere in sea-spray aerosols (SSAs). Recently, there has been considerable interest in the coupling between biological processes and the organic matter content of SSA (O'Dowd et al. 2004, 2015; Quinn et al. 2014; Brooks and Thornton 2018), which provides insights into both the formation and complexity of marine aerosols. Several studies have investigated the impact of SSAs on the TCs, Shpund et al. (2019) found increased CCN concentration near the eyewall region, corresponding to higher cloud water content and concentration of ice hydrometeors, and resulted in higher TC intensity. On the other hand, Carrio and Cotton (2011) used the Regional Atmospheric Modeling System (RAMS), which included the source of SSAs and investigated virtually seeding CCN impacts on an idealized TC. They found that increasing CCN near the rainband region suppresses collision and coalescence processes, increases supercooled water content, and enhances convection near the rainband that reduces the energy supply to the eyewall region, resulting in suppression of TC intensity.

Dust is one of the most abundant aerosol species, since more than 4500 Teragram (Tg) of dust is emitted into the atmosphere on an annual basis (Hu et al. 2019). Saharan

desert is the largest dust emission source, with an estimated 400 to 2200 Tg of dust particles lifted annually (Huneeus et al. 2011). Approximately 25% of this emissions are transported westward to the Atlantic Ocean (d'Almeida 1986; Kaufman et al. 2005; Schepanski et al. 2009; Shao et al. 2011). The Saharan dust outbreak events peak from June to September, which coincides with the Atlantic hurricane season from June to November. Saharan dust exhibits large influences on the genesis and intensification of Atlantic tropical cyclones by modulating cloud hydrometeor contents, diabatic heating distribution, and thermodynamic structure of tropical cyclones (e.g. Dunion and Velden 2004; Sun et al. 2009; Chen et al. 2010, 2015). Dust particles directly absorb and scatter solar radiation, i.e., the dust radiative effect, emit longwave radiation, and change the atmospheric vertical temperature profile (Carslaw et al. 2013; Huang et al. 2015) by cooling the surface, but warming aloft (Carlson and Benjamin 1980; Chen et al. 2010), and play an important role in determining the regional radiative budget (Wang et al. 2013). Ma et al. (2012) found that the dust radiative effect enhances the condensational heating and elevated the zonal and eddy kinetic energy promoting local convection. Moreover, the dust effects on clouds are also sensitive to the relative location of dust to clouds. Dust located above (below) the clouds may suppress (invigorate) convection, due to the dust heating (Koch and Del Genio 2010). Dunion and Velden (2004); Reale et al. (2014) found that the dust radiative effect increased the atmospheric stability and produced less favorable environment to tropical cyclogenesis. Reale et al. (2014) similarly found that dust increases the static stability of the atmosphere and reduces the upward moisture flux from the lower to middle troposphere, leading to a lesser conductive atmosphere for TC

genesis. In addition, Lau and Kim (2007a) found that the dust absorption of solar radiation accounts for 30%–40% of the observed sea surface temperature (SST) change over the Atlantic Ocean between 2005 and 2006. Similarly, Evan et al. (2011); Evan et al. (2006); Evan et al. (2008); Wang et al. (2012) showed an anticorrelation between number of dust outbreaks and the possibility of tropical cyclogenesis, also suggesting that dust reduced SST as a mechanism to inhibit TC activities. On the other hand, Bretl et al. (2015) indicated both enhancing and inhibiting influences of dust radiative effects and little change on TC genesis between active and inactive dust radiative effects.

In addition, Zhang et al. (2007) evaluated the influence of Saharan dust as CCN on the development of idealized TCs using the RAMS and showed that dust induces variations in the hydrometeor properties, modifying the storm diabatic heating distribution, thermodynamic structures, and dynamical responses. The mean sea level pressure (MSLP) at the peak intensity increases by about 25 hPa in the dust-polluted case (2000 cm^{-3}), as a result of invigorated precipitation in the rainband (Zhang et al. 2007; Zhang et al. 2009). Additionally, dust is the most common type of INPs (Isono et al. 1959). DeMott et al. (2003) found that the concentration of INPs is up to 100 times higher in Florida during the Saharan dust episode. It has been shown that both naturally and anthropogenic dust can significantly reduce cloud particle size, optical depth, and liquid water path (Huang et al, 2006a, 2006b, 2010).

The Saharan dust outbreak are associated with a hot and dry well-mixed layer, i.e., Saharan Air Layer (SAL), propagating downstream over the North Atlantic Ocean. (Tao et al. 2018) investigated the microphysics and radiative effects of dust on SAL and has

found that the dust radiative effect results in a drier and warmer SAL. In addition, with the inclusion of dust radiative and microphysical effects, there is a weaker and southward shift of the intertropical convergence zone (ITCZ) and stronger African Easterly Jet (AEJ) that could affect the non-developed AEW. Most recently, Pan et al. (2018) used the Community Atmospheric Model (CAM5) to investigate the radiative and microphysical properties of Saharan dust on the Atlantic regional climate and TCs. The Saharan dust exhibits noticeable impacts on the regional longwave and shortwave radiation, cloud formation, and the convective systems over West Africa and the Tropical Atlantic. The AEJ and West African monsoon are modulated by dust, leading to northward shifts of the ITCZ and the TC genesis region. The dust events induce positive midlevel moisture and entropy deficit anomalies, enhancing the TC genesis. On the other hand, the increased vertical wind shear and decreased low-level vorticity and potential intensity by dust inhibit TC formation in the genesis region. The ventilation index, which is the ratio between vertical wind shear, entropy deficit, and potential intensity, indicating the impacts of environmental wind shear on TC genesis and intensification (Tang and Emanuel 2012), shows a decrease in the intensification region and an increase in the genesis region by dust, corresponding to favorable and unfavorable TC activities, respectively (Figure 6). This dissertation will continue to investigate the detailed microphysical and radiative effects of dust on hurricanes at genesis and intensification stages.

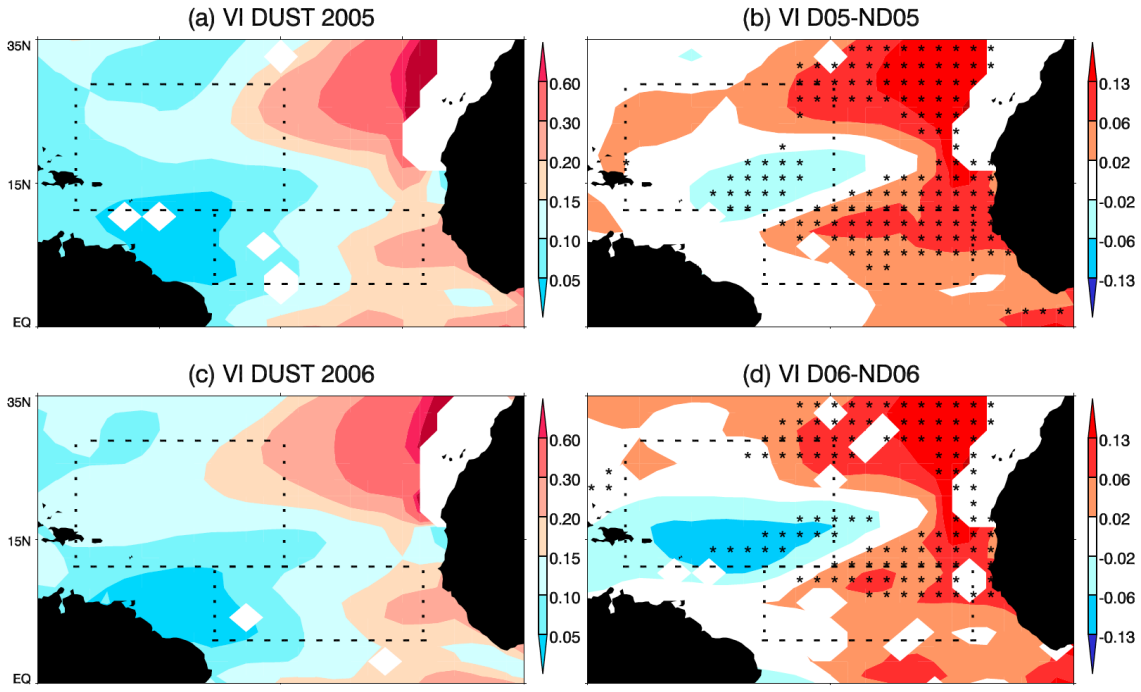

Figure 6: Ventilation Index in 2005 (a) and 2006 (c), and the difference between the dust and non-dust scenarios in 2005 (b) and 2006 (d) from Pan et al. (2018).

In this dissertation, research has been conducted to investigate the impacts of aerosols on the Atlantic TCs. The main objective of the dissertation is divided into two parts: the impact of industrialization on Hurricane Harvey (2017) and the impact of Saharan dust on Hurricanes Danielle and Earl (2010).

The first part of this dissertation investigated the effect of anthropogenic aerosols during Hurricane Harvey (2017). Hurricane Harvey (2017) originally generated from the West African coast on August 15, rapidly intensified on late August 23 after entering the Gulf of Mexico, and made landfall near Rockport, Texas, as a category 4 hurricane. Harvey produced heavy rainfall of about 555 mm in the Houston urban area during 25-28 August. Combined measurements and model simulations were made to show

fundamentally altered cloud microphysical and thermodynamic processes of Hurricane Harvey by anthropogenic aerosols. Ground- and satellite-based lightning and ground-based radar reflectivity measurements were analyzed, showing highly intense lightning and radar reflectivity in the Houston region during 26-27 August. The observations reveal unusually intense lightning (over 0.23 million strikes) and precipitation in the proximity of Houston industrial areas, and these hotspots exhibit a remarkable geographic similarity to a decadal climatological maximum of lightning flash density in the south-central U.S (Orville et al. 2001). A CR-WRF model was used to investigate the effects of aerosols on precipitation and lightning. The ensemble simulations spanned from 25 to 28 August, covering the most intense precipitation periods in the Houston region. The simulations indicate that anthropogenic aerosols increase precipitation and lightning in Houston by a factor of 2-3, unraveling the dominant factor of regulating the energetics and flooding during this weather extreme.

The second part of the dissertation assessed the impact of dust on Hurricanes Danielle and Earl (2010). Hurricane Danielle originated from West Africa coast on August 18 and reached its peak intensity at 18 UTC 27 August, and became a tropical storm on 18 UTC 30 August. Hurricane Earl formed on August 23 and reached hurricane intensity on 12 UTC 29 August. These hurricanes developed under a similar large-scale environment, but were in different stage of their life cycles. Both hurricanes were subjected to the intrusion of Saharan dust and were considered to assess the microphysical and radiative effects of Saharan dust on the genesis and development of TCs in this dissertation. The Weather and Research Forecasting model version 3.6 (WRFV3.6) was used in conjunction with an

aerosol-aware two-moment bulk microphysics scheme, including both the dust ice nucleation effect and the radiative effect of dust. The simulations include three scenarios: with no dust (CTRL), with dust serving as INPs (DSTIN), and both dust as INPs and dust radiative effect (DRAD). The model simulations reveal that the radiative effect of dust significantly decreases (increases) low-level temperature (mid-level moisture). Specifically, DRAD decreased the low-level temperature gradient near the West African continent, suppressed thermal wind balance, and weakened the AEJ. The change in the temperature field perturbs the large-scale circulation, favoring a stronger mid-level ridge in the DRAD scenario which alters the tracks of Hurricanes Danielle and Earl. On the other hand, DSTIN had little impact on dynamical fields, such as vertical wind shear and the large-scale environmental flow. Analyses of Danielle and Earl show a relatively undisturbed Danielle and a significantly suppressed Earl in DRAD. This is possibly because of the highly asymmetric and shallow vortex due to the high environmental wind shear, as well as a significantly lower latent heating rate in DRAD, during the intensification of Earl, resulting in significantly higher minimum central pressures compare to CTRL and DSTIN. Dust serving as INPs enhances the formation of ice hydrometeors and increases the diabatic heating rate above the freezing level in both DSTIN and DRAD. DSTIN slightly suppresses the intensity of Danielle owing an enlarged size of the TC, but did not significantly perturb the intensity of Earl.

This dissertation is organized according to the following outline. In chapter II, a numerical modeling study by utilizing the CR-WRF model are discussed to investigate the role of industrialization on the catastrophic precipitation during Hurricane Harvey. In

chapter III, a series of sensitivity studies were performed to evaluate the impact of radiative and microphysical effects of dust on two Atlantic TCs. Chapter IV summarizes the main findings from this dissertation and provides a closing remark along with potential future research.

2. INDUSTRIALIZATION AS THE DETERMINANT FOR HURRICANE HARVEY'S CATASTROPHE

2.1 Introduction

Hurricane Harvey (2017) originally generated from the West African coast on August 15, but did not develop into a hurricane until it entered the Gulf of Mexico. On late August 23, Harvey started to rapidly intensify as it moved into a region with extremely warm water and light vertical wind shear. It initially made landfall 5 n mile east of Rockport, Texas, as a category 4 hurricane with maximum winds at 115 knots and minimum pressure at 937 mb. Harvey then moved slowly northwestward as it stalled in between two mid-level high pressure systems on August 26 to August 27. Though the intensity of Harvey greatly decreased during this time period, Harvey exerted an unprecedented amount of rainfall near the Houston metropolitan region. Unlike previous Hurricanes Alison (2001) and Beulah (1967) which made landfall at a similar location, the maximum amount of rainfall in Harvey happened near the rainband away from the center of Harvey. Hurricane Harvey is the most costly hurricane to make landfall in the U.S. history with more than $125 billion loss.

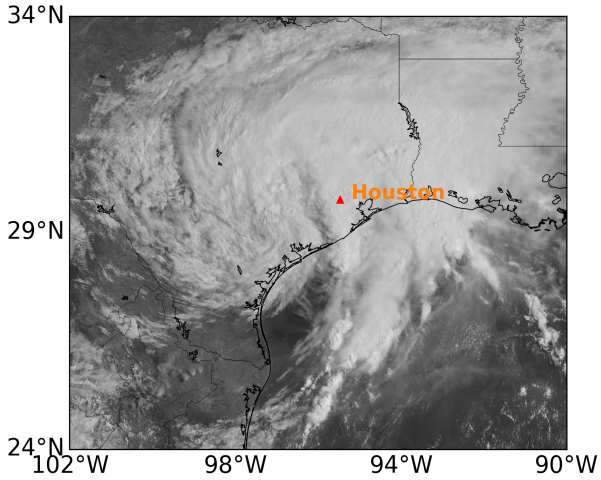

Figure 7: GEOS-16 visible satellite image at 1504 UTC 27 August 2017. The red triangle shows the Houston location.

The spatial distribution and intensity of precipitation from Hurricane Harvey have drawn broad attention. It wreaked havoc on southeast Texas with heavy rainfall of about 555 mm in the Houston urban area (29.5-30.0°N, 95.9-95.2°W) during 25-28 August 2017. As a large and complex low-pressure system associated with high surface enthalpy flux (Figure 7), its development, intensity, and precipitation were regulated by several environmental parameters, including SST, vertical wind shear, vorticity, and humidity of the free troposphere (Emanuel 2017). Several recent studies have linked Hurricane Harvey's devastation to climate change (Emanuel 2017; Trenberth et al. 2018; van Oldenborgh et al. 2017; Wang et al. 2018) or changes in land use due to urbanization (Zhang et al. 2018). In particular, human-caused climate changes were implicated for apparently increasing the intensity and destruction of hurricanes in recent decades, by inducing favorable environmental conditions (such as a higher SST) to supercharge hurricanes and increasing the risk of major damage (Emanuel 2005; Emanuel 2017;

Goldenberg et al. 2001; Patricola and Wehner 2018; Trenberth 2005; Trenberth et al. 2018; van Oldenborgh et al. 2017; Wang et al. 2018; Webster et al. 2005). However, whether the characteristics of hurricanes have changed or will change under a warming climate remains controversial (Knutson et al. 2010). In addition, urbanization causes changes in land use, which were attributed to an increase by about 21 times in the probability of extreme flood events along this highly urbanized coastal area (Zhang et al. 2018). Another key feature of TCs is reflected by efficient formation of hydrometeors and large latent heat release to fuel the development and destruction, i.e., storm surge, strong winds, and flooding. The amount of precipitation in the Houston urban area alone during this extreme event corresponds to an energy of about 5.5 x 10^{18} J released from water condensation - an equivalence of about ninety thousand nuclear bombs dropped in Hiroshima and Nagasaki, Japan, during World War II. Currently, the key factors in determining the destructive power of TCs have yet to be unambiguously established.

From a microphysical perspective, the phase transformation of water molecules from vapor to liquid or ice is non-spontaneous and hindered by profound thermodynamic (free energy) and kinetic (curvature) barriers (Zhang et al. 2015). For example, homogeneous formation of a 10-nm water droplet requires a supersaturation with respect to liquid water (S_w) of at least 0.24 (Zhang et al. 2015), which is too high to achieve in warm clouds (typically less than 0.01). The presence of aerosols is needed to act as CCN for cloud formation, precipitation, and storm development (Fan et al. 2018; Wang et al. 2011).

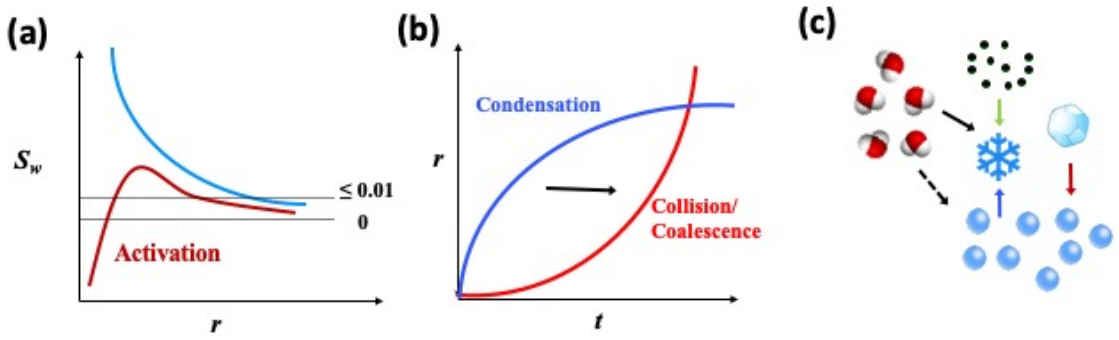

Figure 8: Formation of hydrometeors in clouds: (a) aerosol activation, (b) growth of cloud droplets by condensation and collision and coalescence processes in the warm regime, and (c) growth of mix-phase hydrometeors in the cold regime.

The formation of hydrometeors occurs in the warm regime (T > 0°C) and in the cold regime (T < 0°C). Formation of warm precipitation involves aerosol activation as CCN, condensational growth of cloud droplets, and collision/coalescence growth of cloud droplets to form rain drops (Figure 8). Aerosol activation as CCN depends on the supersaturation (S_w) in cloud and the aerosol properties (i.e., size, chemical composition, or hygroscopicity). In Figure 8 (a), the horizontal lines (i.e., $0 < S_w < 0.01$) label the typical range of supersaturation in warm clouds. The black and blue curves depict S_w as a function of radius (r) for a pure water droplet and an aerosol droplet according to the Kelvin and Köhler theories, respectively. As shown in Figure 8 (b), the growth of cloud droplets in the warm regime includes condensation (blue curve), and collision/coalescence growth (red curve). The condensation growth, i.e., $dr/dt \propto (1/r, S_w)$, is fast for small sizes, but slow for large sizes. On the other hand, the collision and coalescence of cloud droplets, i.e., $dr/dt \propto r^2$, is slow for small sizes, but fast for large sizes. Condensation growth of cloud droplets (~10-20 μm) to reach rain drops (~1 mm) is too slow at small S_w, and the

formation of warm precipitation requires transition from condensation to collision/coalescence growth (black arrow). Hydrometeor formation in the cold regime involves mixed-phase processes. As shown in Figure 8 (c), aerosol (black dots) can act as INPs and form ice hydrometeors (green arrow). Additionally, precipitation formation in the cold regime includes vapor condensation to supercooled droplets (dash black arrow), vapor deposition to ice (solid black arrow) and accretion of supercooled droplets by ice (riming – red arrow).

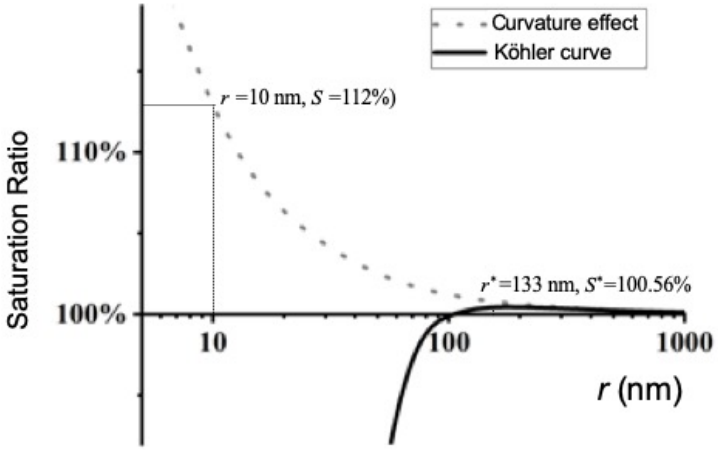

Figure 9: Köhler curve on the activation of sodium chloride and saturation ratio of pure water droplets

Figure 9 shows a comparison of supersaturation for activation of a sodium chloride particle with a dry radius of 20 nm to the ratio of the equilibrium vapor pressure over a pure water droplet to the saturation vapor pressure over a plane water surface. The supersaturation of the sodium chloride particle (0.0056) is much smaller than that of pure water droplets (0.12), indicating the presence of aerosols is essential for cloud formation.

There has been accumulating evidence that natural and anthropogenic aerosols play critical roles in the genesis and development of TCs (Fan et al. 2016; Herbener et al. 2014; Khain et al. 2010; Pan et al. 2018; Rosenfeld et al. 2012; Tao et al. 2011; Wang et al. 2014; Zhao et al. 2018). A previous modeling study demonstrated that high aerosol levels invigorate rainbands and increase precipitation, but decrease the eyewall strength (Wang et al. 2014). Another recent observational analysis also corroborated that anthropogenic aerosols enlarge the rainfall area of TCs over the northwestern Pacific (Zhao et al. 2018). However, most operational forecast models simulate the track and intensity of hurricanes using microphysics schemes with a prescribed number concentration of cloud droplets to represent the formation and growth of hydrometeors, which are insensitive to the aerosol microphysical effects (Zhang et al. 2018; Zhang et al. 2016). Also, the number concentrations of CCN/cloud droplets in those models are typically fixed at levels characteristic of pristine maritime environments (Zhang et al. 2018; Zhang et al. 2016), but significantly underrepresented over land, particularly in urban and industrial areas (Zhang et al. 2015).

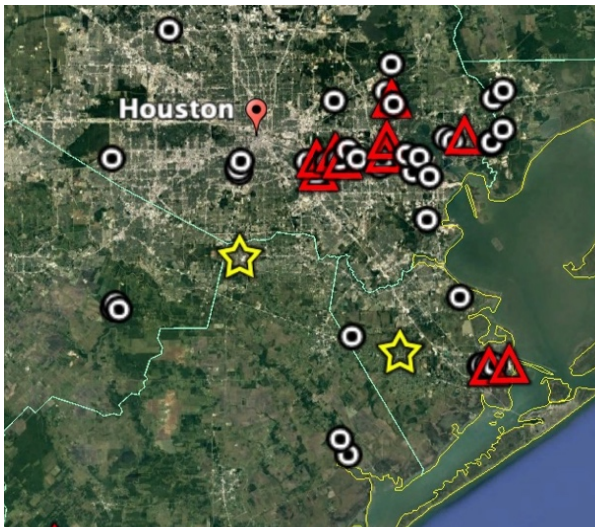

Figure 10: Power plants (white circles) and petroleum refineries (red triangles) location near Houston, Texas.

In addition to being the country's fourth largest city, Houston hosts many industrial facilities, i.e., power plants, chemical manufactories, and petroleum refineries (Zhang et al. 2015) (Figure 10). In particular, this region is home to one of the world's most densely distributed (over 400) refineries, which comprise approximately 40% of the nation's petrochemical capacity with a daily production of 0.3 million barrels. In addition, there are many (~175) offshore rigs in the Gulf of Mexico region. Measurements in the Houston industrial areas showed that the average mass concentration of $PM_{2.5}$ (particulate matter smaller than 2.5 μm) has exceeded the annual average of the National Ambient Air Quality Standards (Fan et al. 2005; Levy et al. 2013; Zhang et al. 2015). Furthermore, ground-based measurements and model simulations showed that industrial emissions of anthropogenic aerosols considerably influence convection, lightning, and precipitation in Houston (Li et al. 2009; Li et al. 2008; Orville et al. 2001; Williams et al. 1991).

2.2 Methods

2.2.1 Weather Research and Forecasting (WRF) model simulations

The Advanced Research Weather Research and Forecasting model version 3.6 (ARW WRFv3.6) was used for Hurricane Harvey simulations. The WRF model simulation was initialized at 0600 UTC 23 August 2017, and assimilated brightness temperature from the Geostationary Operational Environmental Satellite (GOES-16) were used from 0600 UTC 23 August to 0000 UTC 25 August. The free-run simulation covered the period from 0000 UTC 25 August to 0000 UTC 28 August with two two-way nested vortex-following domains and horizontal grid spacings of 27 km, 9 km, and 3 km. Table 1 shows the model setup for the two scenarios.

<table>
<tr><td rowspan="5">Model Physics</td><td colspan="3">Microphysics: TAMU Two-moment bulk microphysics</td></tr>
<tr><td colspan="3">Surface Layer Options: Mellor–Yamada Nakanishi Niino (MYNN) Scheme</td></tr>
<tr><td colspan="3">Planetary Boundary Layer Physics: Yonsei University Scheme (YSU)</td></tr>
<tr><td colspan="3">Radiation: RRTMG Shortwave and Longwave Schemes</td></tr>
<tr><td colspan="3">Cumulus parameterization : Kain–Fritsch Scheme for outer domain</td></tr>
<tr><td rowspan="3">Scenarios</td><td colspan="3">Land Surface Model: 5–layer Thermal Diffusion Scheme</td></tr>
<tr><td>C-case</td><td>Ammonium sulfate 209/cm^3</td><td rowspan="2">sea-spray aerosols (60/cm^3)</td></tr>
<tr><td>P-case</td><td>Ammonium sulfate 4192/cm^3</td></tr>
</table>

Table 1: Model configuration and scenarios setup for the simulation of Harvey

An aerosol-aware two-moment microphysics scheme was used in the CR-WRF simulations. The mass-mixing ratio and number concentration of aerosols were predicted. Aerosols activated as CCN according to the Köhler theory once the supersaturation criteria were reached (Li et al. 2008). The microphysical scheme calculated the mass-mixing ratios

and number concentrations of five different types of hydrometeors, including cloud water, rain water, ice crystal, snow, and graupel. The Kain-Fritsch cumulus parameterization was only used on the outer most domain (Kain 2004). All domains used the Rapid Radiative Transfer Model for Global Climate Models (RRTMG) scheme to calculate both shortwave and longwave radiations (Iacono et al. 2008), and the Yonsei University Scheme (YSU) was used to determine the physical characteristics in the planetary boundary layer and at the surface (Hong et al. 2006). The sea-surface temperature for the free-run was initiated from the Optimum Interpolated daily sea-surface temperature (Banzon et al. 2016).

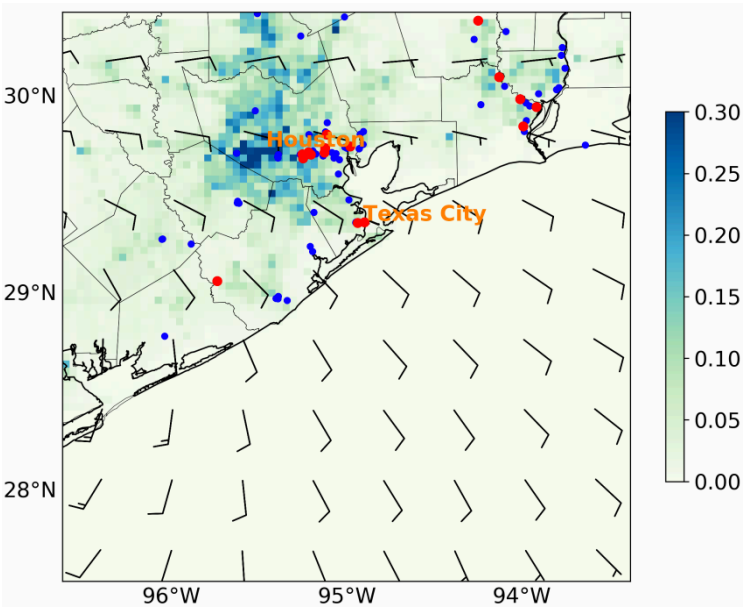

Figure 11: $PM_{2.5}$ mass concentration (μg m^{-2} s^{-1}) on 27 August 2017. Red dots represent the petroleum refineries, and the blue dots are the power plants. The wind barbs are the 1000 mb wind in ERA5.

Two scenarios, a clean (C-case) and a polluted case (P-case), were considered to realistically represent the concentration, emission, and distribution of natural and

anthropogenic aerosols over the model domain. Aerosols in both cases consisted of anthropogenic aerosols and SSAs. The initial concentrations of anthropogenic aerosols in the Houston urban area were 209 and 4192 cm^{-3} for the C- and P-cases, respectively, according to field measurements in the Houston urban area (Levy et al. 2013). These initial concentrations of anthropogenic aerosols in the Houston urban area, along with the aerosol optical depth (AOD) measured by the Moderate Resolution Imaging Spectroradiometer (MODIS) from 17 to 24 August, were used to derive the geographic distribution of anthropogenic aerosols in the outer domain (8° S - 52° N, 13 – 118° W). Specifically, the initial concentrations of anthropogenic aerosols for the C- and P-cases at a grid-point over land were calculated by multiplying the aerosol concentrations in the Houston urban area for the two cases to the ratio of the values of the local to Houston AOD over the outer domain. The initial concentrations of anthropogenic aerosols over ocean were determined according to the same procedure, except that smaller aerosol concentrations (by ten times) were applied to the Houston values to reflect the land and ocean contrast. The SSA was uniformly distributed over land and ocean with the initial concentrations of 6 and 60 cm^{-3}, respectively. A sea salt production scheme was included, where SSA was produced according to the wind speed (Wang et al. 2014). In addition, a constant emission rate of 46 kg s^{-1} was implemented to the bottom 1 km of the atmosphere in the Houston urban area to account for continuous emission of anthropogenic aerosols during Hurricane Harvey. Such an aerosol emission rate was close to half of that (105 kg s^{-1}) from the National Emission Inventory in the Houston urban area (Figure 11). The SSA consisted of mainly sea salt with a hygroscopic parameter (κ) value of 0.9, and the anthropogenic

aerosols had a κ value of 0.53, characteristic of the aerosol hygroscopicity measured in the Houston region (Levy et al. 2013). The removal of aerosols included activation to form cloud droplets, but precipitation scavenging was not considered in the present simulations.

Supersaturation is expressed as $S_w = \exp(\frac{2\sigma M_w}{rRT\rho_w})$ (Kelvin equation) for a pure water droplet and $S_w = a_w \exp(\frac{2\sigma M_w}{rRT\rho_w})$ (Köhler theory) for an aerosol particle, where $\sigma, M_w,$ and ρ_w are the surface tension, molecular weight, and density of water, respectively, R is the gas constant, T is temperature, and a_w is the water activity in the aerosol phase. The hygroscopicity parameter (κ) is defined as (Zhang et al. 2012),

$$1/ a_w = 1 + \kappa\frac{V_d}{V_w} \qquad \text{(Equation 1)}$$

where V_d and V_w are the volumes of the dry aerosol and water, respectively.

The vertical distribution of SSA and anthropogenic aerosols followed an exponential decay function, with the highest concentration at the surface. For each aerosol scenario, five ensemble simulations were performed, where the initial temperature field was randomly perturbed.

2.2.2 Lightning Potential Index (LPI)

The LPI was calculated to reflect charge generation and separation, based on the ratios of ice and liquid water and the kinetic energy of the storm between 0°C and −20°C levels. The LPI is calculated from the simulated vertical velocity (ω; m s^{-1}) and mass mixing ratios (kg kg^{-1}) of liquid water (q_l), rain (q_r), ice (q_i), snow (q_s), and graupel (q_g) according to equation (2). V is the volume of air between 0°C and −20°C in m^3. ε is

defined in equation (3), where Q_l represents the total liquid water mass mixing ratio ($q_l + q_r$; kg kg $^{-1}$). Q_i is the ice fractional mixing ratio (kg kg $^{-1}$, equation 4).

$$\mathrm{LPI} = \frac{1}{V}\iiint \varepsilon\, \omega^2 \mathrm{dx\, dy\, dz} \quad (2)$$

$$\varepsilon = {2(Q_i Q_l)^{0.5}}\Big/{(Q_i + Q_l)} \quad (3)$$

$$Q_i = q_g\left[\left({(q_s q_g)^{0.5}}\Big/{(q_s + q_g)}\right) + \left({(q_i q_g)^{0.5}}\Big/{(q_i + q_g)}\right)\right] \quad (4)$$

2.2.3 Lightning and radar reflectivity measurements

The observed rainfall data was taken from the Stage IV Precipitation NCEP/EMC 4KM Gridded Data (Lin et al. 2011). The lightning source points and lightning events data were from the Houston Lightning Mapping Array (HLMA, Cullen 2018) and Geostationary Lightning Mapper (GLM) from the GOES-16 (GEOS-R working group, 2018) .

The observed rainfall data was taken from the hourly Stage IV Precipitation NCEP/EMC 4KM Gridded Data. The Stage IV precipitation analysis was based on a combination of surface rain gauge measurements and radar calculated rainfall produced by twelve River Forecast Centers (RFCs) in the Contiguous United States. Each RFC manually quality controls the Multisensor Precipitation Estimates (MPE) precipitation data in its respective region before being included in the national Stage IV mosaic. The hourly analyses were used in this work.

The lightning source points and lightning events data were from the Houston Lightning Mapping Array (HLMA), National Lightning Detection Network (NLDN), and GLM on GOES-16. The HLMA is a three-dimensional total lightning location system that includes twelve lightning detection stations within 200 km of Houston, providing total lightning mapping for the Houston region and southeast Texas. Each station includes a Very High Frequency (VHF, 60 MHz) time-of-arrival total lightning mapping sensors built by the New Mexico Institute of Mining and Technology (Cullen 2018). The sensor detects the time of arrival of a VHF impulse emitted as part of the electrical breakdown and lightning propagation process. Data from each sensor are processed on a central LMA server to provide three-dimensional mapping of these impulses, i.e., LMA sources. The GLM, on board of the GOES-16, is a single-channel, near-infrared optical transient detector that can detect the momentary changes in an optical scene, indicating the presence of lightning. GLM measures the frequency, location and extent of lightning discharges, as well as total lightning activities (in-cloud, cloud-to-cloud and cloud-to-ground) with a near-uniform spatial resolution of approximately 10 km (GEOS-R working group, 2018). The NLDN consists of over 100 remote, ground-based sensing stations located across the U.S. that instantaneously detect the electromagnetic signals when lightning strikes occur (Orville et al. 2001). The spatial and temporal distributions of the LMA sources, NLDN strikes, and GLM level 2 lightning events were used in our analysis.

The vertical cross-section and maximum radar reflectivity data were from the three-dimensional gridded Next Generation Weather Radar (NEXRAD) (Bowman and

Homeyer, 2017), i.e., the Weather Surveillance Radar, 1988, Doppler (WSR-88D) network.

2.3 Results

We analyzed ground- and satellite-based lightning (Figure 12) and ground-based radar reflectivity (Figure 13), showing highly intense lightning and radar reflectivity in the Houston region (27-32 °N, 94-98°W) during 26-27 August.

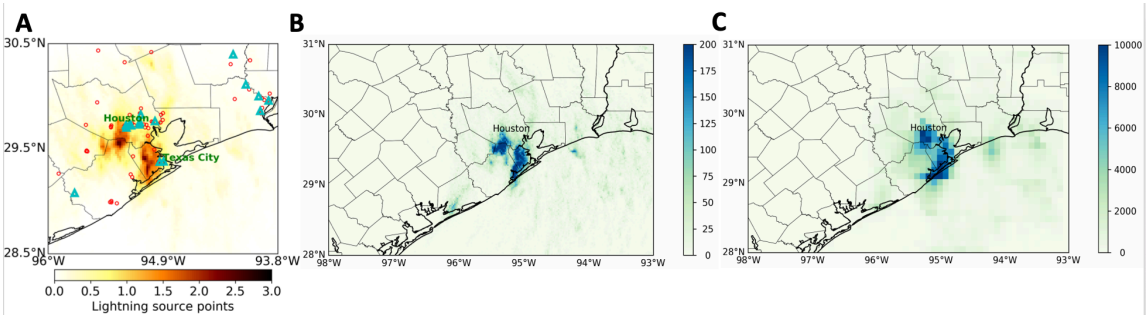

Figure 12: Lightning density (10^{-4} points per km^2) from 25 to 27 August from Houston Lightning Mapping Array (A), National Lightning Detection Network (flash per 4 km^2) (B), and Geostationary Lightning Mapper (events per 81 km^2) (C).

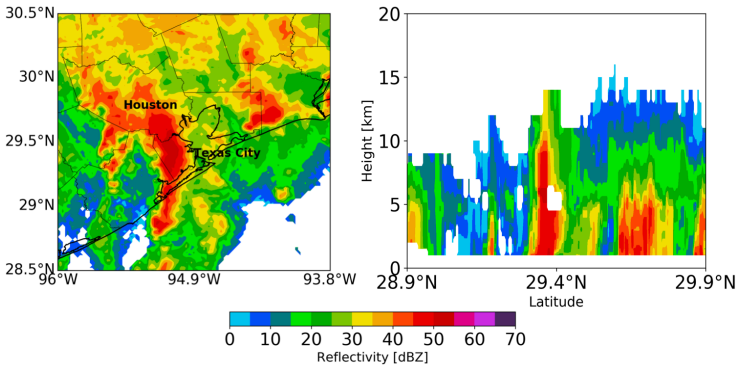

Figure 13: Base radar reflectivity in dBZ (left), and vertical cross-section of radar reflectivity in dBZ (right) at 0510-0515 UTC 27 August.

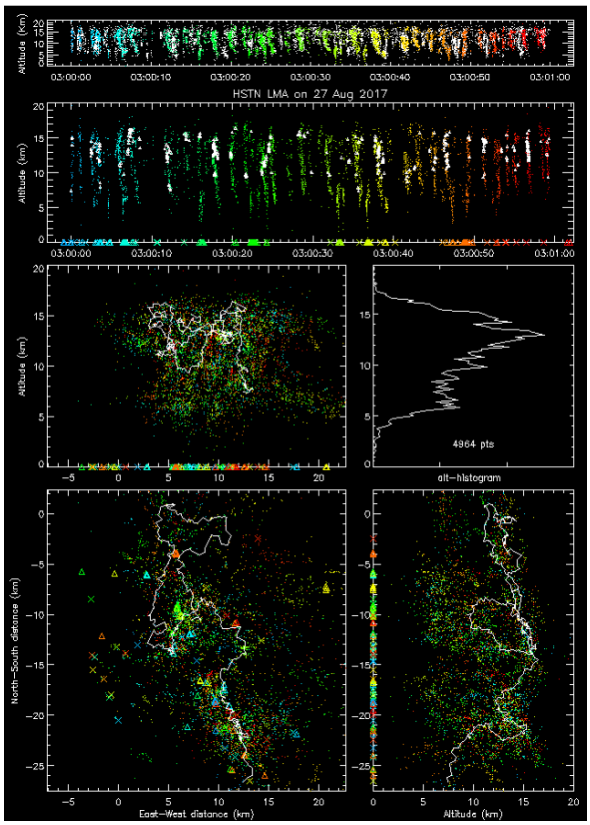

Figure 14: A long lightning strike during 0300 UTC and 0301 UTC August 27. Figure by Claire Onak.

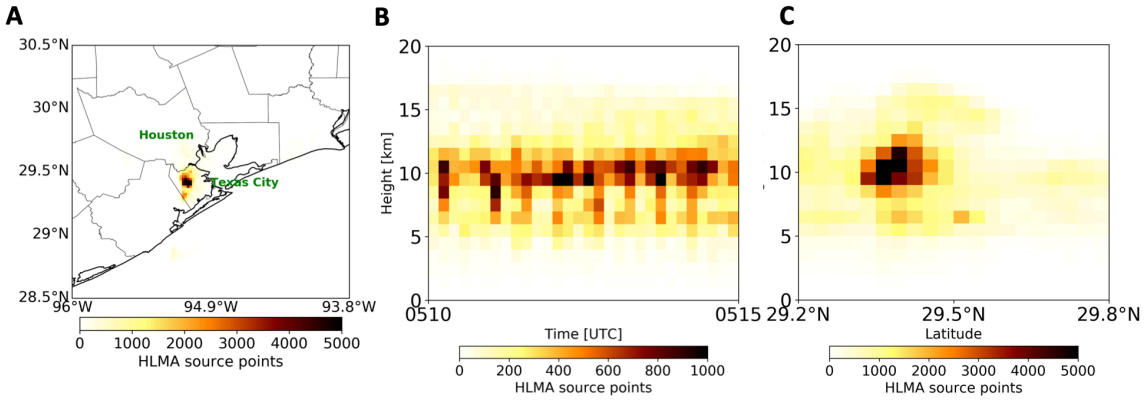

Figure 15: An active storm episode during 0510-0515 UTC 27 August: horizontal distribution of HLMA lightning source points (A), vertical zonal cross-section of HLMA lightning source points (B), vertical time series of HLMA lightning source points (C). HLMA source points unit is frequency per 4 km^2.

Measurements by the three-dimensional HLMA (Figure 12A), and NLDN (Figure 12B), and GLM Satellite (Figure 12C) exhibited a similar spatiotemporal pattern of unusually active lightning at the location surrounded by the Houston industrial facilities. A total of 0.23 million (intracloud and cloud-ground) lightning strikes were detected by the NLDN from 26 to 28 August, and over 12 million lightning source points were recorded by HLMA during 26-27 August. Also, the lightning flashes exhibited large horizontal and vertical extensions. For example, an individual lightning strike with a horizontal dimension exceeding 138.4 km occurred between 0300 UTC and 0301 UTC 27 August (Figure 14). From 0510 to 0515 UTC on 27 August, the most active lightning occurred at 29.4° N and 95.1° W (Figure 15A) and extended vertically from 5 to 15 km, with the maximum intensity at 10 km (Figure 15B and C). The lightning hotspot (Figure 15B) collocated with the maximum radar reflectivity (Figure 13A). The vertical cross-section of radar reflectivity (Figure 13B) showed the maximum value of 50 dBZ reaching up to 10 km height, indicating strong precipitation and convective activity. Furthermore, the geographic distributions of the lightning hotspot detected by the GLM, HLMA and NLDN and the accumulative precipitation maximum (Figure 12 and Figure 16) during this event exhibited a striking similarity to a decadal climatological maximum lightning flash density in the south-central U.S. (Figure 16B), which was attributed to the aerosol effects from Houston industrial emissions .

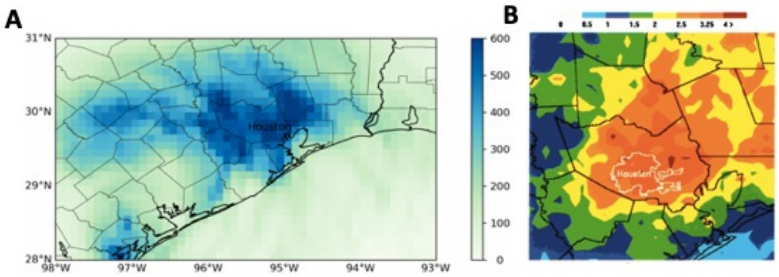

Figure 16: (A) NCEP Stage IV accumulated precipitation (mm) from 1200 UTC 25 August to 0000 UTC 28 August. (B) Climatological distribution of lightning flash density (flash per km^2) in Houston from 1989 to 2000 from NLDN (Orville et al. 2001).

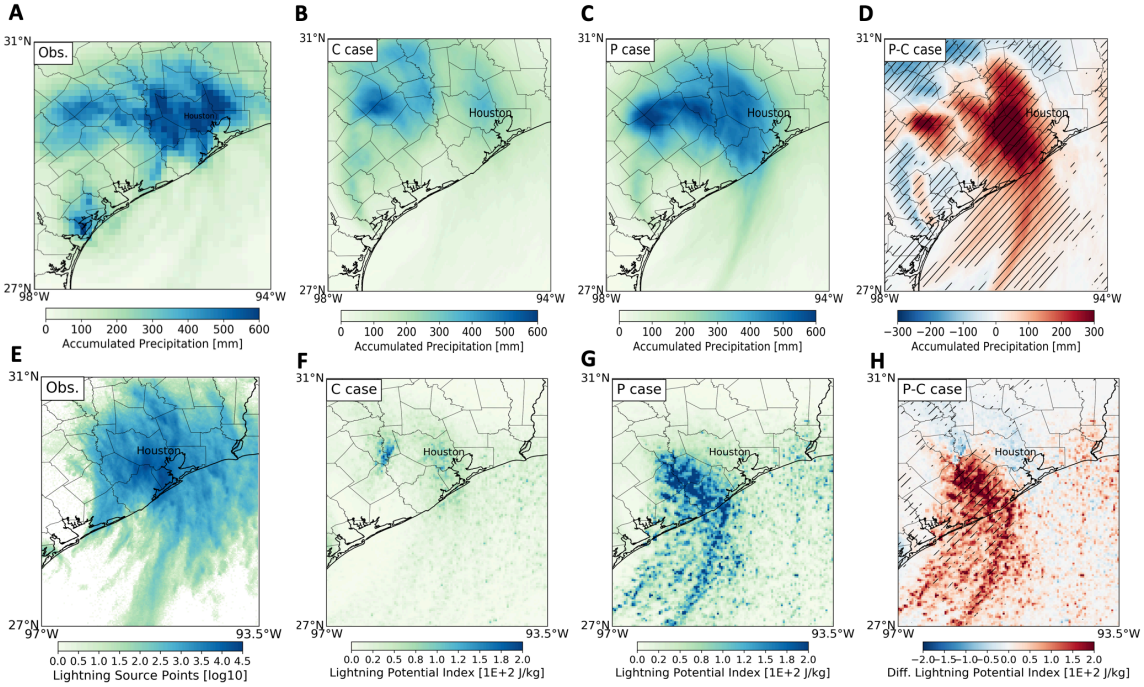

Figure 17: Aerosol effects on precipitation and lightning. (A to D) Observed and simulated accumulative precipitation (mm) from 0000 UTC 26 August to 0000 UTC 28 August: observation from the NCEP Stage IV data (A), P-case (B), C-case (C), and the difference between P and C cases (D). (E) HLMA lightning source points ($\log_{10}$) from 0000 UTC 26 August to 0000 UTC 28 August. (F to H) Simulated LPI from 0000 UTC 26 August to 2330 UTC 27 August: P-case (F), C-case (G), and the difference between the P- and C-cases (H). Hatched lines denote the significant difference between the P- and C-cases according to the Student's t-test at the 95% confidence level.

We quantified the effects of aerosols on precipitation (Figure 17, A to D) and lightning (Figure 17, E to H) using a CR-WRF model. The ensemble simulations spanned from 25 to 28 August, covering the most intense precipitation periods in the Houston region. Sensitivity studies were performed under two aerosol scenarios, i.e., a clean (C) and a polluted (P) case, representative of the aerosol concentration, emission, and distribution of the pristine condition similar to those used in the operational forecast models (Zhang et al. 2018; Zhao et al. 2018) and elevated anthropogenic aerosols from industrial sources in the Houston region (Fan et al. 2005; Levy et al. 2013; Zhang et al. 2012), respectively. Simulations of the C- and P-cases show similar spatial distributions, but distinctly different magnitudes in precipitation. The accumulative precipitation during 26 and 28 August are much higher in the P-case than in the C-case, (Figure 17, B and C), and the difference between the two cases ranges from 100 to 350 mm in the Houston urban area (Figure 17D). The distribution and magnitude of precipitation in the P-case are consistent with those from the observation (Figure 17A), while precipitation is significantly under-predicted in the C-case. Also, we calculated a LPI to reflect charge separation and generation relevant to cloud electrification (Orville et al. 2001). The LPI is highly elevated in the P- case, but minimal in the C-case (Figure 17, F and G), with the largest difference by a factor of 3 (Figure 17H). The distribution of enhanced LPI in the P-case is also comparable to the observed lightning pattern (Figure 17E).

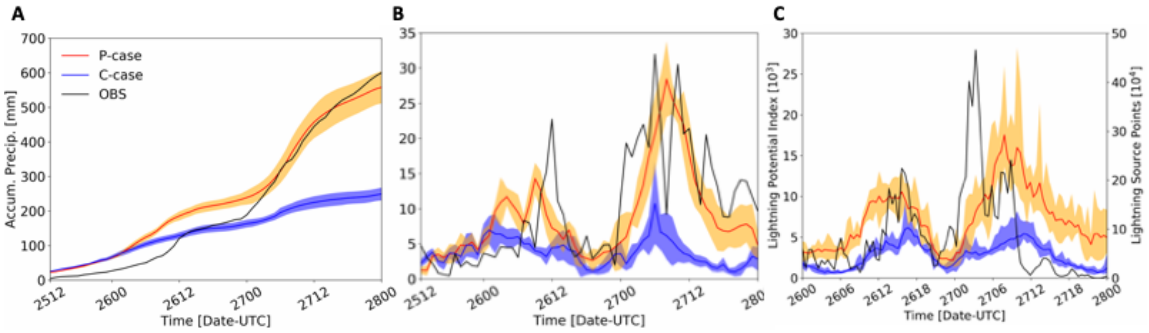

Figure 18: (A and B) Temporal evolution of the accumulative precipitation (A, mm) and precipitation rate (B, mm hr^{-1}) in the Houston urban area from 1200 UTC 25 to 0000 UTC 28 August, showing two intense precipitation periods, i.e., during 1000 UTC – 1300 UTC 26 August (Rain I) and 0000 – 1800 UTC 27 August (Rain II). The black curve corresponds to the measurements, and the blue and red curves denote the simulations in the C- and P-Cases, respectively. (C) Observed temporal evolution of lightning source points (10^4) by HLMA from 0000 UTC 26 August to 2330 UTC 27 August and simulated LPI (10^3) in C- (blue) and P-Case (red) in the Houston region. The shaded area denotes the range of deviation from the ensemble simulations.

The temporal evolution of the accumulative precipitation in the Houston urban area during 25 and 28 August is comparable between the observation and P-case, with the values of 558 ± 47 mm and 600 mm, respectively (Figure 18A). In contrast, the accumulative precipitation (249 ± 19 mm) in the C-case is less than half of those of the observation and P-Case. The observed and simulated precipitation rates exhibit two intense periods (Figure 18B). The maximum precipitation rate in the P-case is 28 ± 5 mm hr^{-1}, in agreement with the observation (32 mm hr^{-1}), and both values are about a factor of 3 higher than that (11 ± 6 mm hr^{-1}) in the C-case. The temporal evolution of the simulated LPI in the P- and C-cases are similar to the observation, while the LPI value is 2.8 times higher in the P-case than in the C-case (Figure 18C).

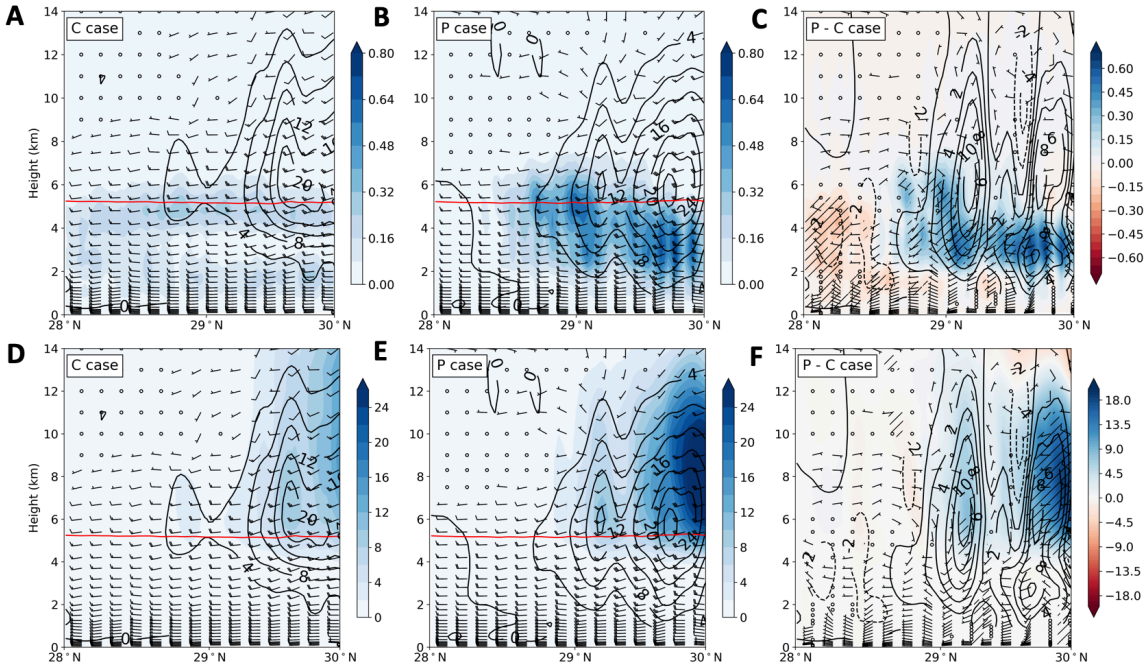

Figure 19: Simulated vertical cross-section of ice and liquid water contents over the Houston region. (A to F) Averaged vertical cross-section (95.2 - 95.9° W) in the Houston urban area for liquid water path (A to C, color shaded in g m^{-2}) and ice water path (D to F, color shaded in g m^{-2}) and latent heating rate (contour line in K day^{-1}) at 0500 UTC 27 August: C-case (A, D), P-case (B, E), and the difference between P and C cases (C, F). The hatched lines represent the 95% confidence levels according to the Student's t-test. The red line in A, B, D, and E labels the freezing level, which is about 5.3 km.

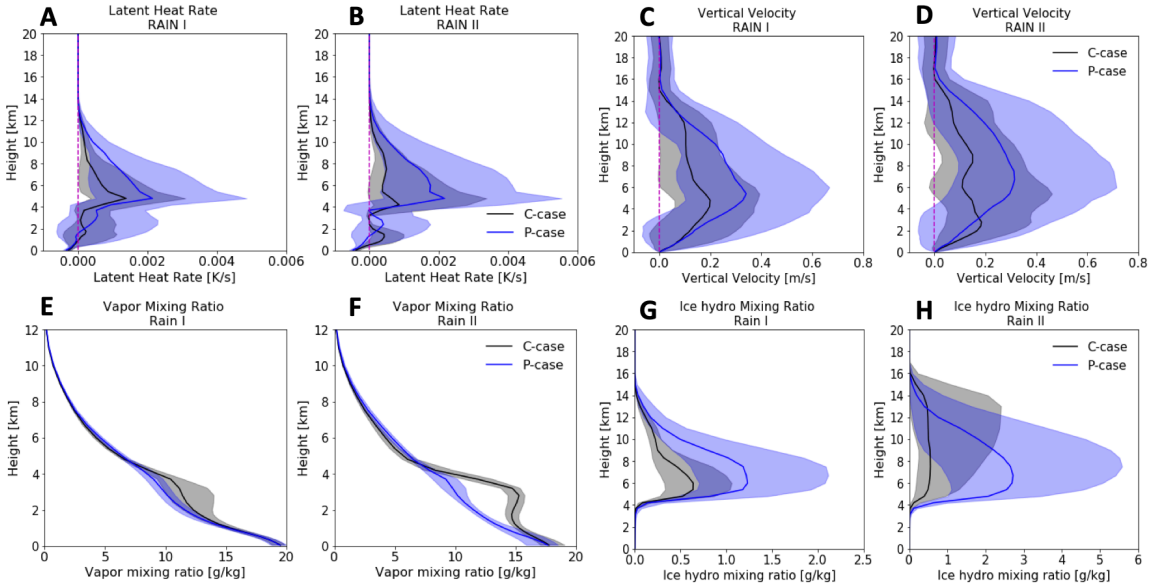

Figure 20: Contoured-frequency-by-altitude diagrams (CFADs) of latent heating rate, vertical velocity, and mixing ratios of hydrometeors. (A and B) Latent heating rate (K s^{-1}). (C and D) vertical velocity (m s^{-1}). (E and F) water vapor mixing ratio (g kg^{-1}). (G and H) mixing ratio of ice hydrometeors (g kg^{-1}). Black and blue lines represent the C- and P-cases, respectively. The solid lines correspond to the 50th percentile values, and the shaded areas represent the 25th and 75th percentiles. The panels A, C, E, and G represent the first period of heavy rainfall (1000-1300 UTC, 26 August, RAIN I), and the panels B, D, F, and H represent the second period of heavy rainfall (0000-1800 UTC, 27 August, RAIN II). The values are calculated in the Houston urban area during the two periods of heavy rainfall.

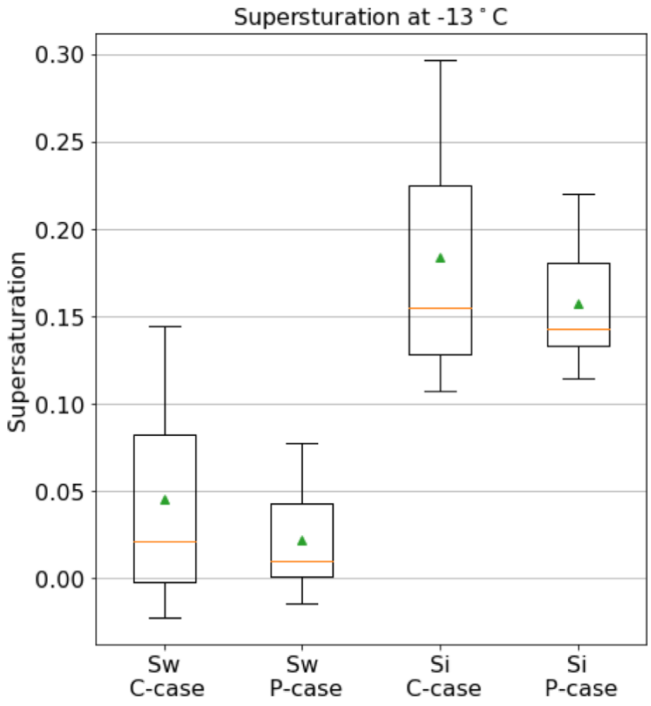

Figure 21: Simulated supersaturation ratio with respect to liquid (S_w) and ice (S_i). The supersaturation ratios for the P- and C-cases are averaged from 1100 UTC 25 to 0000 UTC 28 August in the Houston urban area. The boxplots represent the 25th and 75th percentile of the values, and the whiskers represent the 5th and 95th percentiles of the values. The green triangles and the orange lines represent the mean and median values, respectively.

To gain insight into the cause of the aerosol-induced storm invigoration, we analyzed the microphysical characteristics of hydrometeors and latent heating profiles in the model simulations. The vertical cross-sections of mixing ratios of liquid and ice hydrometeors in the P-case are highly elevated between 2-4 km and 6-12 km, respectively, and large latent heat is released between 4-8 km (Figure 19, A, B, D, and E). The largest difference in the latent heating rates between the P- and C-cases is up to 10 K day^{-1} (Figure 19, C and F), corresponding to an increase of 250% in the P-case. The averaged vertical distributions of mixing ratios and latent heating rates for hydrometeors in the Houston urban area show higher values of both quantities in the P-case than in the C-case during

the two intense precipitation periods (Figure 20, A, B, G, and H). Latent heat release is linked to vapor condensation to cloud droplets in the warm regime (> 0°C) and vapor condensation/deposition to supercooled water/ice in the mixed-phase regime (< 0°C), both of which are dependent on supersaturation (S_w or S_i). In addition, freezing of supercooled droplets releases a smaller amount latent heat of fusion (about 11-12% of those for vapor condensation/deposition). Supersaturation (S_w or S_i) is produced by vertical lifting because of decreasing temperature, but is consumed by vapor condensation/deposition, while the minimum Si value in the mixed-phase regime is constrained by the difference in the saturation vapor pressures between supercooled water and ice. The maximum latent heat rate in the P-case is about two-fold higher than that in the C-case, because of more efficient vapor condensation in the warm regime. Similarly, the average S_i and S_w values in the P-case are 0.16 and 0.03 at -13°C or 7 km (Figure 21), indicating condensational/depositional growth of supercooled water/ice hydrometeors and continuous latent heat release in the mixed-phase regime (albeit dominated by the ice process). The high supersaturation (S_w and S_i) below/above the freezing level is attributed to strong cyclonic lifting and abundant moisture supply (Figure 21). The S_w and S_i values in the mixed-phase regime are higher in the C-case than in the P-case, because of lesser vapor depletion with fewer hydrometeors. Similarly, efficient condensation of water vapor to form cloud droplets in the warm regime reduces the vapor mixing ratio between 2-4 km in the P-case (Figure 20, E and F). Condensation in the warm regime and condensation/deposition/riming in the mixed-phase regime are higher in the P-case, resulting in about 2 times larger latent heating rate and updraft velocity (Figure 20, C and

D). Hence, the increases in liquid/ice contents, latent heating rate, and vertical velocity in the P-case contribute importantly to localized enhancement of precipitation and lightning in the Houston region (Figure 17 and Figure 20).

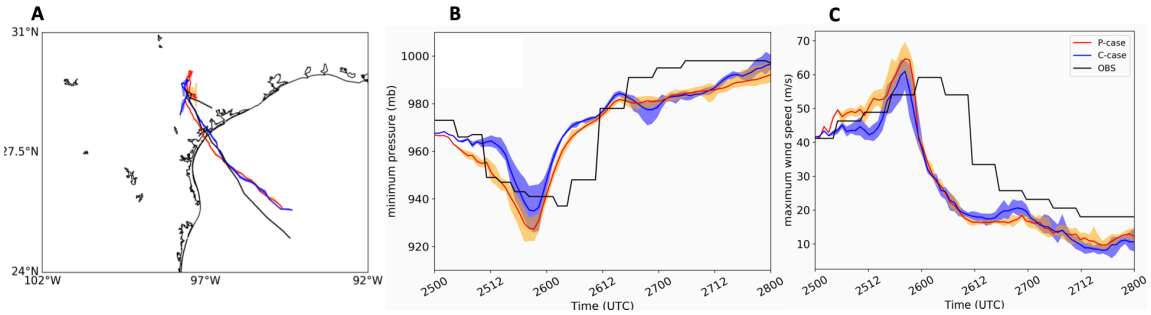

Figure 22: (A) Comparison of the storm tracks between the observation and simulation in the C- (blue) and P-Case (red). (B and C) Comparison of the minimum pressure (B, mb) and maximum wind speed (C, m s^{-1}) between the observation and simulation in the C- (blue) and P-Case (red). The shaded area (in B and C) denotes the range of deviation from the ensemble simulations.

Our simulations well reproduce the track (defined by the minimum surface pressure) and intensity (defined by the minimum surface pressure and the maximum wind speed) during the storm evolution, especially considering the first landfall near Corpus Christi and stalling across inland Texas. The simulated track is insensitive to the aerosol perturbations (Figure 22A). A comparison of the minimum pressures and maximum wind speeds between the P-and C-cases shows a slightly lower surface pressure and higher wind speed, respectively, in the P-case (Figure 22B and C). The minimal aerosol effects on the storm track and intensity are in contrast to the common notion that elevated aerosols considerably reduce the eyewall strength, development, and the intensity of hurricanes (Fan et al. 2016; Herbener et al. 2014; Hu et al. 2019; Khain et al. 2010; Pan et al. 2018;

Rosenfeld et al. 2012; Tao et al. 2011; Wang et al. 2014). On the other hand, both observation and simulations reveal distinct structures and intensity for precipitation, lightning, and radar reflectivity (Figure 12-15, Figure 17 and 18). Noticeably, there is an absence of the well-defined eyewall and symmetric rainband, but the presence of localized intense precipitation, lightning, and radar reflectivity (Figure 7 and Figure 16). These storm features are uncharacteristic of hurricanes, but are explainable by spatially inhomogeneous storm invigoration by aerosols.

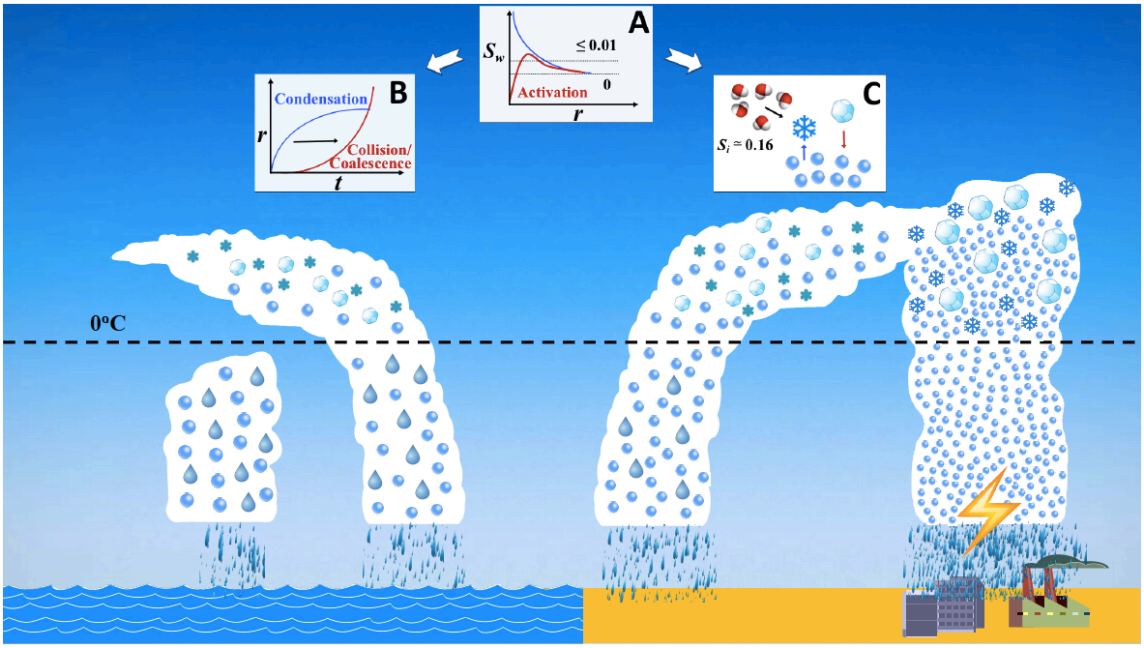

Figure 23: A microphysical perspective of aerosol-induced storm invigoration. (A) Aerosols activate as CCN in warm clouds (i.e., $0 < S_w < 0.01$ labeled by the horizontal dashed lines). The black and blue curves depict S_w as a function of radius (r) for a pure water droplet and an aerosol droplet according to the Kelvin and Köhler theories, respectively. (B) Warm precipitation includes condensation (blue curve, $dr/dt \propto 1/r$) and collision/coalescence growth (red curve, $dr/dt \propto r^2$) of cloud droplets, which are fast (slow) for small (large) sizes and are slow (fast) for small (large) sizes, respectively. Condensation growth of cloud droplets (~10 μm) to reach rain drops (~1 mm) is too slow because of small S_w, and warm precipitation requires transition from condensation

to collision/coalescence growth (black arrow). (C) Mixed-phase precipitation includes vapor deposition to ice and accretion of supercooled droplets by ice (riming). Ice deposition is significantly more efficient in the mixed-phase regime because of higher S_i (with an average value of 0.16 in the P-case at 7 km), forming snowflakes (by deposition) that further grow to large graupels by riming. For cloud formation from left to right, increasing aerosol levels result in suppressed warm precipitation (i.e., inhibited A to B conversion) but favorable mixed-phase processes (i.e., enhanced A to C conversion). The aerosol-hindered warm precipitation is related to formation of higher concentrations of size-uniform smaller cloud droplets, which inhibit collision/coalescence. However, vapor condensation is more efficient at a higher aerosol level, producing more latent heat release and stronger buoyancy. In addition, a suppressed warm rain is essential to maintaining the storm strength, since falling of rain drops would otherwise reduce the updraft relevant to the buoyancy (from condensation of cloud droplets) and cyclonic lifting. In the absence of warm precipitation, cloud droplets are effectively transported above the freezing level to promote the growth of ice hydrometeors by deposition and riming, leading to enhanced latent heat release and large ice hydrometeors.

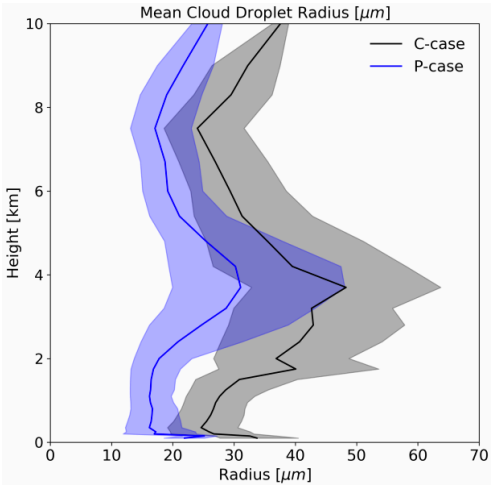

Figure 24: CFADs of mean cloud droplets radius. The simulated mean radius (μm) of cloud droplets from 1100 UTC 25 to 0000 UTC 28 August in the Houston urban area. Black and blue lines are the 50th percentile values in the C- and P-cases, respectively. The shaded areas represent the 25th and 75th percentiles.

Our combined measurements and simulations reveal that the extreme precipitation and lightning during Hurricane Harvey are attributed to anthropogenic aerosols, which profoundly alter the cloud microphysical and thermodynamic processes (Figure 23).

Elevated aerosol levels from the industrial sources act as CCN (Figure 23A) to produce more numerous and uniformly-distributed, but smaller cloud droplets in the warm regime (Figure 24). Although condensation of cloud droplets produces larger latent heat release in the P-case, collision/coalescence of cloud droplets is effectively inhibited by a narrow distribution of higher numbers, but smaller sizes (Figure 23B). The enhanced buoyancy and inhibited rain formation in the warm regime facilitate vertical lifting and promote the mixed-phase processes, leading to more efficient growth of ice hydrometeors by vapor deposition and riming in the P-case (Figure 23C). The combination of higher contents of liquid/ice hydrometeors (Figure 19), larger latent heat release (Figure 20, A and B), and stronger updraft velocity (Figure 20, C and D) significantly modifies the storm structures and energetics from the C- to P-cases (Figure 23). Clearly, the remarkable similarity in the geographic distributions between the extreme flooding/lightning during this event and the maximum lightning flash density from the decadal climatology in the Houston region (Orville et al. 2001) is not a coincidence (Figure 12, B to C), and our work provides the compelling microphysical and thermodynamic evidences for anthropogenic aerosols as the determinant in regulating the energetics and destruction during Hurricane Harvey.

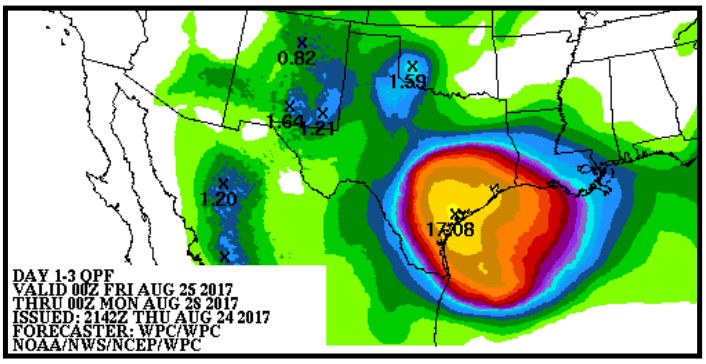

Figure 25: 72-hour quantitative precipitation forecast (QPF) by the NOAA Weather Prediction Center. Accumulative precipitation forecast from 0000 UTC 25 to 0000 UTC 28 August, 2017 by the NOAA Weather Prediction Center, produced from a constitution of 46-member ensembles.

Forecast by the U.S. National Weather Service during this event produced major discrepancies from the observation (Figure 25). Our results demonstrate that this disparity in the predicted precipitation is associated with the inability of the operational forecast models to account for the aerosol effects (Fan et al. 2018; Peng et al. 2016). Also, industrial sources may produce elevated levels of primary ultrafine particles (Huang et al. 2015) to contribute to the storm damage, via an analogous invigoration mechanism (Fan et al. 2018). Furthermore, it is also plausible that industrialization-inducing flooding during Hurricane Harvey is exacerbated under climate change (Emanuel 2017; Fan et al. 2018; Trenberth et al. 2018; van Oldenborgh et al. 2017) and/or urbanization (Fan et al. 2018). This former dominant role discovered in our study underscores the importance of representing the effects of anthropogenic aerosols for accurate short-term forecast and climate projection of TCs to minimize future catastrophic destruction along the highly-industrialized Gulf of Mexico region.

3. QUANTIFICATION OF DUST IMPACT ON DIFFERENT STAGES OF TROPICAL CYCLONES, DANIELLE AND EARL (2010)

3.1 Introduction

Dust is one of the most abundant aerosol species with an annual global emission of 1000 to 4000 Teragram (Tg) (Zender et al. 2004; Huneeus et al. 2011). The Saharan desert is the largest global dust emission source with an estimated 1150 Tg of dust particles lifted annually; approximately 25% of the emissions are transported westward (d'Almeida 1986; Kaufman et al. 2005; Schepanski et al. 2009; Shao et al. 2011) and around 136 – 222 Tg yr^{-1} of dust deposit into the Atlantic Ocean (Yu et al. 2019). Saharan dust outbreak events peak from June to September (Carlson and Prospero 1972), which coincides with the peak of the Atlantic hurricane season (June to November). Numerous studies have shown significant correlations between the amount of Saharan dust emission and Atlantic TC activities, with higher dust emissions correlating with lessened Atlantic TC activities (Lau and Kim 2007a, 2007b; Sun et al. 2009).

Saharan dust exhibits large influences on the genesis and intensification of TCs by modulating cloud hydrometeor content, diabatic heating distributions, and thermodynamic structure (Chen et al. 2015; Dunion and Velden 2004; Sun et al. 2009), as well as large-scale environmental parameters, such as vertical wind shear and mid-level moisture (Pan et al. 2018). Dust particles directly absorb and scatter solar radiation, i.e., the dust radiative effect or dust direct effect, emit longwave radiation, and perturb the atmospheric vertical temperature profile (Carslaw et al. 2013; Huang et al. 2015), causing cooling at the surface

and warming aloft (Carlson and Benjamin 1980; Chen et al. 2010). Dunion and Velden (2004) showed that the dust radiative effect increased the atmospheric static stability which produced a less favorable environment for TC genesis. Similarly, Reale et al. (2014) found that dust increased the static stability of the atmosphere and reduced the upward moisture flux from the lower to middle troposphere, leading to a less conductive atmosphere for TC genesis. Recently, Chen et al. (2017) utilized the WRF-CHEM model and found that radiatively active low-level dust particles increased convective inhibition (CIN) and suppressed TC genesis. Strong et al. (2018) found that the dust radiative effect suppressed TC activities over the North Atlantic Ocean possibly due to the changing of SST, but the detailed mechanism remained unclear. Alternatively, Bretl et al. (2015) used ECHAM6-HAM model and found that the radiative effect of dust had both supporting and inhibiting influences on the large-scale environment for TC genesis. Furthermore, Braun (2010) suggested that unfavorable conditions for TC genesis are introduced by environmental large-scale subsidence, instead of atmospheric flow perturbations owing to the radiatively active dust. In addition to the influence of the dust radiative effect on the large-scale environment, there are numerous studies on the radiative effect of dust on individual TCs. Chen et al. (2015) found that the inclusion of dust radiative effects induced a warm anomaly inside the dust plume and changed of the deep layer steering flow, which likely reduced the forecast error for Hurricane Helene (2006). On the other hand, Nowottnick et al. (2018) found that the strongly absorbing dust dynamical response induced positive temperature perturbations and deviated the track of Hurricane Nadine (2012) from the observed track. Though numerous studies have investigated the radiative

effect of dust on TC genesis, the nature of the radiative effect of dust on TC genesis and development remains unclear.

In addition, dust particles can serve as CCN, INPs, and giant CCN (GCCN), i.e., the dust microphysical effect or dust indirect effect, that modify the cloud macro- and micro-structures and further perturb the hydrological cycle (Seigel et al. 2013). DeMott et al. (2003) found that the INP concentration is up to 100 times greater over Florida during a Saharan dust episode. Jenkins et al. (2008) found observational evidence that Saharan dust served as additional CCN and INPs, increased vertical velocity and cloud water content, and invigorated convective activities. They suggested that dust as INP enhanced the mix-phase microphysical processes and served as a mechanism for enhancing tropical deep moist convection. On the other hand, Rosenfeld et al. (2001) found that dust as CCN reduced cloud-particle effective radii and suppressed precipitation through decreasing coalescence. Similarly, Min et al. (2009), based on observations, found that the dust microphysical effect altered the precipitation size spectrum toward smaller particles, resulting in a decreased precipitation rate and local accumulated precipitation. Zhang et al. (2007); Zhang et al. (2009) utilized the Regional Atmospheric Model System (RAMS) to investigate the response of idealized TCs to dust particles and found an asymmetric eyewall due to the increased vertical wind shear and enhanced cold pool development near the rainband region, causing an up to 22 hPa increase in the minimum pressure and a much larger eye size in the high dust concentration scenario. Shi et al. (2014) investigated both the direct and indirect effects of mineral dust on mesoscale convective systems (MCS) over West Africa and found that the dust indirect effect increased all cloud hydrometeor

concentrations, especially the ice content in the upper troposphere, resulting in a larger anvil coverage. However, when considering both the direct and indirect effects of dust, they found overwhelming influence of the dust direct effect, which delayed the activation of CCN and INP, as well as the onset of the MCS. Tao et al. (2018) utilized the NU-WRF model and found that the dust indirect effect increased the specific humidity north of the dust layer and both direct and indirect effects of dust shifted the ITCZ slightly southward (and corresponding deep moist convection) and reduced both vertical velocity and hydrometeor contents. Huang et al. (2019) simulated a MCS over West Africa and found that dust–radiation effect delayed the formation of the MCS, but enhanced convective activities once it forms. In addition, similar to both Shi et al. (2014) and Tao et al. (2018), they found a dominant role of the dust direct effect rather than the indirect effect on the strength and onset of the deep moist convection. On the other hand, Nowottnick et al. (2018) found that the shortwave aerosol atmospheric forcing was overwhelmed by the longwave cloud atmospheric forcing surrounding Nadine, suggesting that radiative effects resulting from aerosol–radiation interaction are secondary to aerosol–cloud interaction for Hurricane Nadine (2012).

Overall, numerous studies have investigated the radiative effect of dust on the Atlantic regional climate and TC genesis and development. Saharan dust not only stabilizes the atmosphere through the dust radiative effect, but also introduces CCN, GCCN, and INPs that could invigorate deep moist convection by the dust indirect effect. There remains no consensus on the quantitative assessment of the microphysical and radiative effects of dust, both collectively and respectively, on individual TCs. In this

study, we investigate both the radiative and microphysical effects of dust on two individual TCs (Danielle and Earl 2010) within a similar large-scale circulation pattern. The results shed light on the microphysical and radiative effects of dust on the TCs in different stages of their development. Two scientific questions will be addressed in this study:

1) How does the radiative and microphysical effects of dust alter the genesis and development of the two TCs?
2) What is the relative importance of the microphysical and radiative effects of dust on the two TCs?

Our hypothesis is that the microphysical effect of dust changes the local diabatic heating and thus perturbs the intensity of the TCs. The radiative effect of dust changes the atmospheric temperature profile and large-scale circulation, affecting both the track and intensity of the TCs.

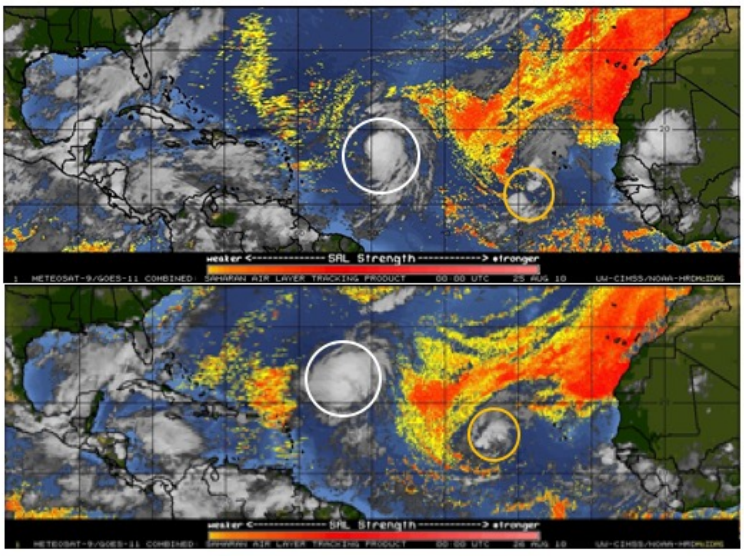

Figure 26: Geostationary Operational Environmental Satellite (GOES)-11 Saharan Air Layer product on 00 UTC 25 Aug 2010 (top) and 00 UTC 26 Aug 2010 (bottom) with Danielle (white circles) and Earl (orange circles). The orange shading denotes the dry and warm air introduced by Saharan dust.

Hurricane Danielle (2010) emerged from the West African coast on 18 August, but did not intensify until 23 August owing to moderate wind shear conditions. Danielle reached a peak intensity at 18 UTC 27 August, but slowly weakened into a tropical storm after 18 UTC 30 August due to the increasing influence of a deep mid-to-upper-level trough and associated increases in deep-layer vertical wind shear. Hurricane Earl initially developed from a strong African easterly wave on 23 August and eventually strengthened into a tropical depression by 06 UTC 25 August. Earl rapidly intensified from 06 UTC August 29 to 00 UTC 30 August and reached hurricane intensity by 12 UTC 29 August. Both hurricanes developed under a similar large-scale environment and displayed interactions with Saharan dust during their course of development (Figure 26).

3.2 Methods

The CR-WRFv3.6 was used in this study. The physics configurations of these simulations are listed in Table 2. The Texas A&M University (TAMU) aerosol-aware two-moment bulk microphysics scheme was implemented in the simulations, which includes thirty-two microphysics processes (Li et al. 2008). The microphysics scheme calculates the mass mixing ratios and number concentrations of five hydrometeors including rain, cloud water, ice, graupel and snow. Currently, the ammonium-sulfate and sea-salt can be activated as CCN once the environment reached supersaturation. The size distribution followed a lognormal distribution, aerosols are distributed into 92 size bins with a maximum radius of 2.5 μm . The vertical distribution of the aerosol follows an exponential decay function. The critical radius of dry aerosols is calculated from the Köhler curve according to vapor mixing ratio output from the model.

Model Physics	Microphysics: TAMU Two-moment bulk microphysics Surface Layer Options: Mellor–Yamada Nakanishi Niino (MYNN) Scheme Planetary Boundary Layer (PBL) Physics: MYNN Level 2.5 and Level 3 Schemes Radiation: Goddard Shortwave Radiation Scheme; RRTMG Longwave Schemes Cumulus parameterization : Grell-Freitas ensemble scheme Land Surface Model: Community Land Model Version 4 (CLM4)	
Scenarios	CTRL	No dust
	DSTIN	Dust (3000/cm^3) Sulfate, sea salt (100/cm3, 60/cm3)
	DRAD	Dust (3000/cm^3)

Table 2: Model configuration and scenarios setup for the simulation of Danielle and Earl

Dust is treated as hydrophobic aerosols and can serve as the INP. The dust follows a lognormal size distribution with radius from 0.25 to 10 μm. A new dust ice nucleation scheme has been implemented into the TAMU microphysics scheme. The activation of dust as INP is related to the temperature and relative humidity (RH) with respect to water and ice, following the Thompson-Eidhammer scheme (Thompson and Eidhammer 2014). When RH with respect to water is greater than 98.5%, INP activation follows (DeMott et al. 2010), which accounts for both the condensation and immersion freezing of particles greater than 0.5 μm. When RH with respect to water is less than 98.5%, INP activation follows (Phillips et al. 2008) accounting for deposition nucleation. The homogeneous freezing of cloud water follows (Milbrandt and Yau 2005). In addition, the radiative properties of dust was implemented into the Goddard Shortwave radiation scheme to account for the dust radiative effect (Fan et al. 2008). The refractive indices are based on Optical Properties of Aerosols and Clouds (OPAC) (Hess et al. 1998). Aerosol particles in the radiation scheme follow a core-shell structure, with dust as the core and ammonium sulfate as the shell. The vertical distribution of dust is shown in Figure 27 (left). Dust is

uniformly distributed across the model domain with an idealized dust emission implemented across the West African continent (Figure 27, right).

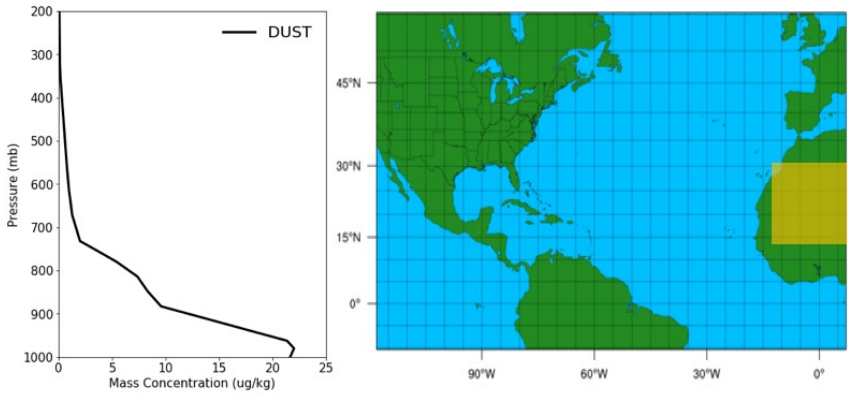

Figure 27: Initial dust vertical distribution for the DSTIN and DRAD scenarios (left); the model domain with an idealized dust emission from West Africa (right).

The simulation utilized 9 km grid spacing with 37 vertical levels and was initialed using the Climate Forecast System Reanalysis (CFSR) data. The model simulations were initiated at 06 UTC 24 August and ended at 06 UTC 30 August and covered the intensification and decay of Hurricane Danielle and genesis and intensification of Hurricane Earl. Hurricane Danielle is initialized using an idealized vortex on 06 UTC 24 August, 2010. In addition, the SST is prescribed from the CFSR and updated every 6 h.

To address the above scientific questions, three sets of simulations, i.e., with no dust effects (CTRL), with dust microphysics effects (DSTIN), and both dust radiative and microphysics effects (DRAD) (Table 2), were established to investigate the microphysical and radiative effects of dust on the genesis and intensification of two hurricanes. Each scenario included five ensemble members each by slightly perturbing the initial temperature field.

3.3 Results

3.3.1 Large Scale Analysis

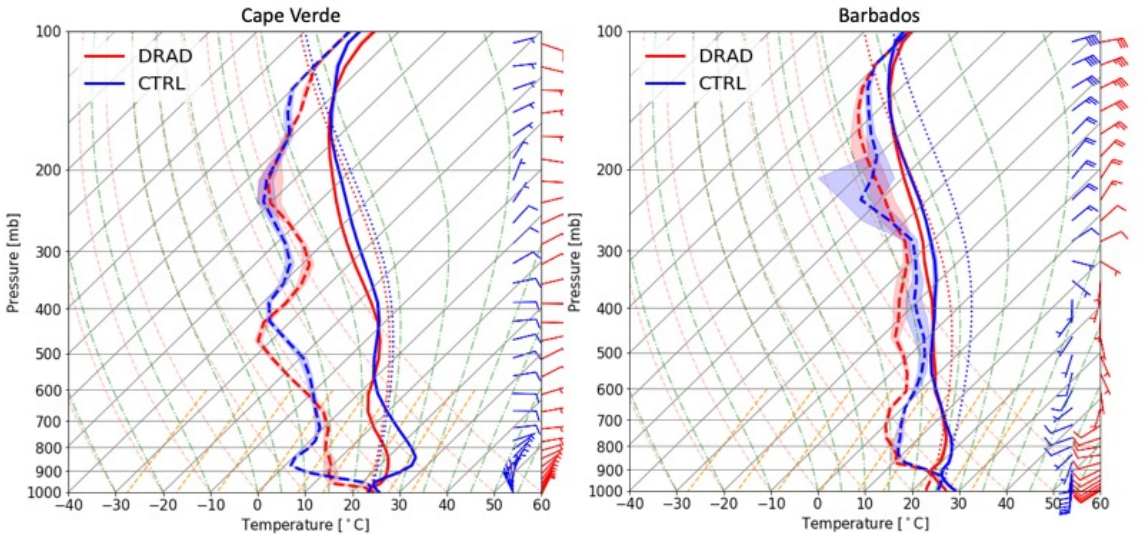

Figure 28: Skew-*T* Log-*p* graph on 18 UTC 27 August from Cape Verde (left) and Barbados (right). The shading area represents the variation among five ensembles. The rightmost solid lines on each graph are the temperature (˚C) and the leftmost dashed lines are the dewpoint temperature (˚C). Horizontal winds are plotted at the right (half barb = 5 m s^{-1}; full barb = 10 m s^{-1}).

Figure 28 shows skew-*T* log-*P* plots from Barbados and Cape Verde at 18 UTC 27 August, when Danielle reached its maximum intensity. The dust radiative effect (DRAD, red lines) shows slightly warmer (cooler) temperatures at 500 mb (300 mb) at both locations. There is up to a 6°C temperature decrease below 600 mb and a slightly warmer temperature at 500 mb at Cape Verde because dust absorbs and reflects incoming shortwave radiation. DRAD also shows fluctuations in the moisture profile owing to slightly decreased RH at around 600 mb in both locations. These variations in temperature and moisture profiles change the CAPE (CIN) from 1259 J/kg (438 J/kg) in CTRL to 1470 J/kg (132 J/kg) in DRAD at Cape Verde, because dust decreases the surface temperature

and reduces the inversion in the lower levels. On the contrary, dust decreases the CAPE from 3489 J/kg in CTRL to 1113 J/kg in DRAD with minimal CIN difference at Barbados owing to possibly little inversion in the lower atmosphere. For the vertical wind profile, DRAD does not show much variation in the wind direction, but displays decreases in the wind speed at around 600 mb. Similarly, Figure 29 shows a weaker AEJ (hatched region) along 15°N between 35°W and 15°W owing to the decrease of the horizontal temperature gradient over the East Atlantic Ocean near the West African continent (color shaded) and a corresponding weakening of thermal wind balance. In addition, Figure 29 shows an amplified 500 mb (orange contours) ridge in the mid-Atlantic Ocean (centered around 50°W and 30°N) at 00 UTC 30 August due to the aforementioned temperature variations induced by southerly flow along 60°W and the warm air advection caused by the dust radiative effect (DIFF, Figure 29). Overall, dust radiative effects decrease the surface temperature and slightly warm the mid-level temperature, as well as change the horizontal temperature gradient, acting to stabilize the atmosphere, weaken the AEJ, and amplify the mid-level ridge. Alternatively, DSTIN does not show much deviation from the CTRL, indicating the insignificant impacts of dust microphysical effects on the large-scale environment.

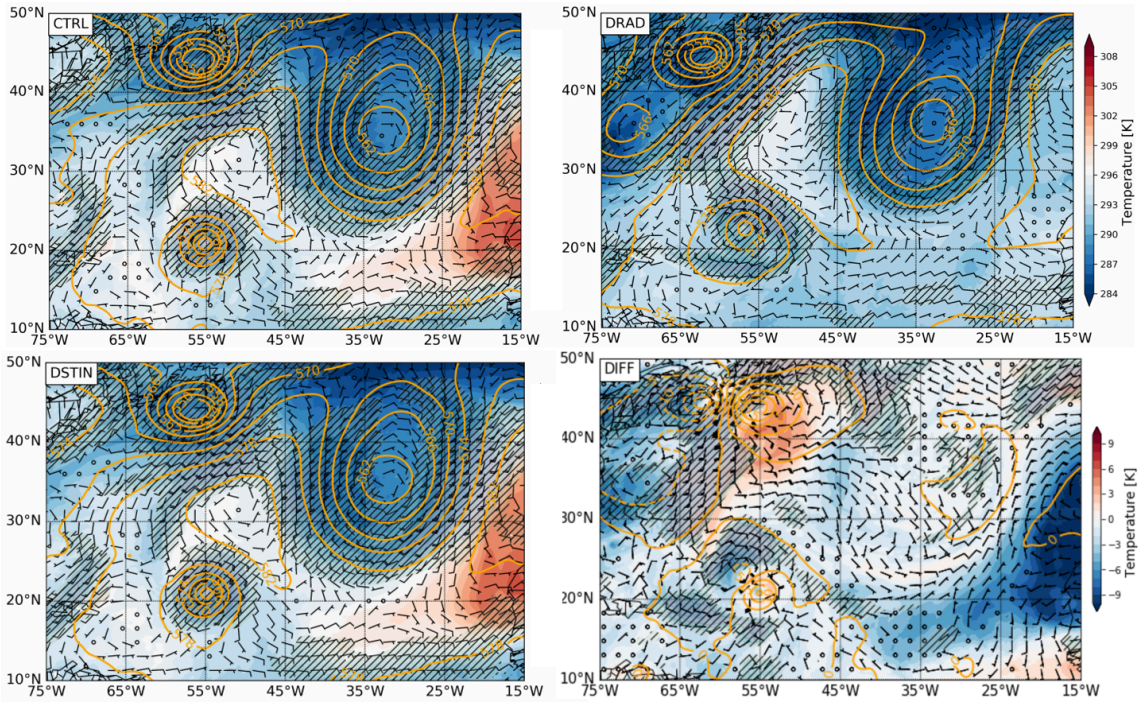

Figure 29: Wind barbs at 600 mb, geopotential height at 500 mb (dam, orange lines), and temperature at 850 mb (K, color shaded) at 00 UTC 30 August, 2010. The hatched lines represent wind speed greater than 10 m s^{-1}. DIFF represents the difference between DRAD and DSTIN.

Potential intensity (PI) is used to assess the impact of dust on the large-scale thermodynamic field. PI, which represents the possibly maximum intensity of a TC, is calculated according to Bister and Emanuel (2002) under pseudoadiabatic assumptions by the following equation 5:

$$\mathrm{Vmax}^2 = \frac{T_s}{T_0}\frac{C_k}{C_D}(\mathrm{CAPE}^* - \mathrm{CAPE})_m \quad (5)$$

, where T_s is the SST (K), and T_0 is the mean outflow temperature at the tropopause (K), C_k is the exchange coefficient for enthalpy, and C_D is the drag coefficient. CAPE (J kg^{-1})

is based upon a parcel of air lifted from the boundary layer in reference to the environmental sounding and CAPE* is a based on a parcel of air lifted from saturation at sea level.

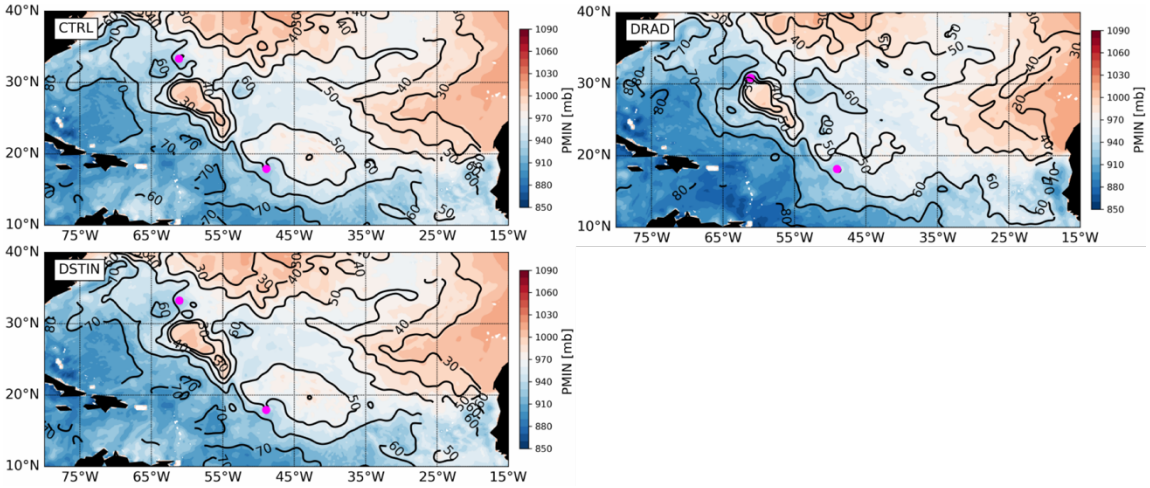

Figure 30: Potential Intensity represented by minimum pressure (color shaded, P_{min} in mb) and maximum wind speed (black contours, V_{max} in m s^{-1}) at 12 UTC 28 August. The magenta dots represent the location of Danielle (north) and Earl (south).

Figure 30 shows the potential intensity represented by maximum velocity (V_{max}, contour lines) and minimum pressure (P_{min}, contour shading) at 12 UTC 28 August. PI is greater over the West Atlantic Ocean due to the warmer SST. In CTRL and DSTIN scenarios, Danielle (the north magenta dot) is located over a higher V_{max} (lower P_{min}) region compared to that of DRAD. Earl (the south magenta dot), on the other hand, is surrounded by a region with relatively lower P_{min} (~936.8 mb) in DRAD, compared to CTRL (~955.3 mb) and DSTIN (~954.8 mb), indicating that DRAD had more favorable thermodynamic conditions for the development of Earl. This is possibly due to the decreasing of the low-level specific humidity that increases the difference between

CAPE* and CAPE in DRAD. Figure 31 shows the bulk wind difference between 200 and 850 mb (color contours; proxy for vertical wind shear) and water vapor mixing ratio at 900 mb at 12 UTC 29 August. DRAD shows an asymmetric distribution of vertical wind shear around Earl and greater than 20 m s^{-1} of vertical wind shear (blue contours) on the east side of Earl between 55-45°W, 20-30°N (Figure 31b). CTRL and DSTIN, on the other hand, show a symmetrically high vertical wind shear pattern around Earl, indicating storm-induced wind shear and relatively lower vertical wind shear magnitudes around Earl. These changes in vertical wind shear possibly hinder the intensification of Earl in DRAD. Alternatively, the vertical wind shear shows no significant difference between the DSTIN and the CTRL (Figure 31a and c).

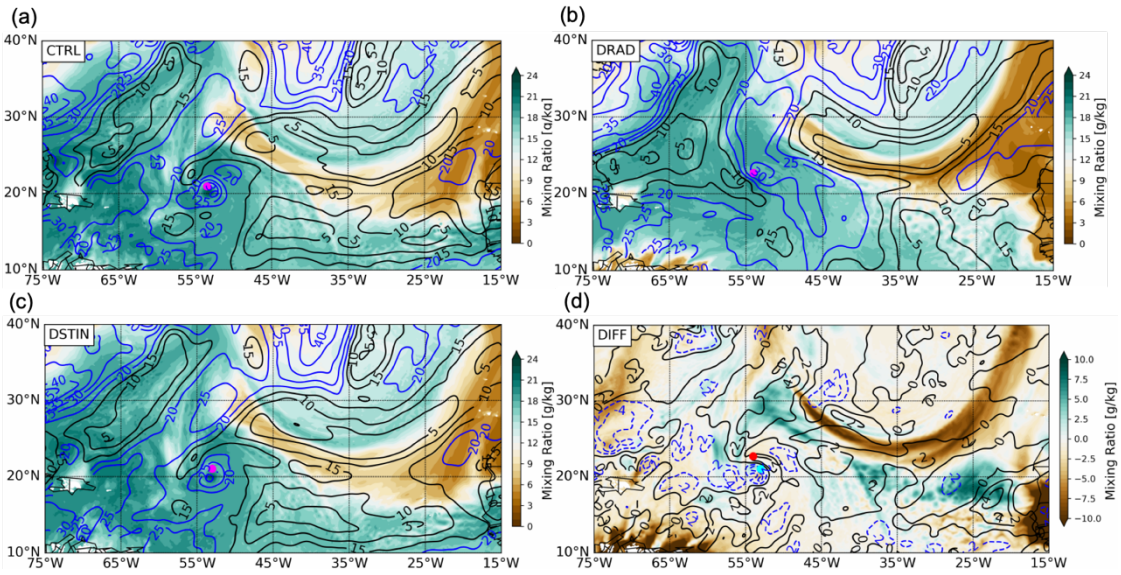

Figure 31: Vapor mixing ratio (shading, g kg^{-1}) at 900 mb and vertical wind shear between 850 mb and 200 mb at 12 UTC 29 August 2010. The blue contours show the wind shear value greater than 20 m s^{-1}. The magenta color dots represent the location of Earl. The red and cyan dots in (d) represent the DRAD and DSTIN, respectively. DIFF represents the variation between DRAD and DSTIN.

Overall, DRAD shows decreases in low-level temperatures, a weakening of the AEJ, and amplification of the ridge system in the mid-Atlantic region. In addition, DRAD displayed thermodynamically (dynamically) favorable (unfavorable) conditions for the development of Earl by increasing PI (increasing deep-layer vertical wind shear). DSTIN does not show significant impacts on the large-scale environment.

3.3.2 Hurricane Danielle

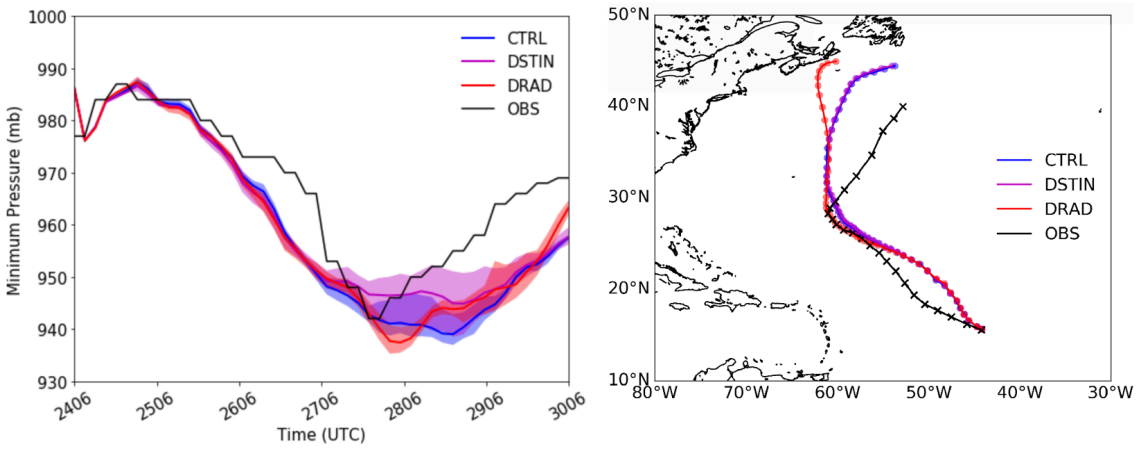

Figure 32: Minimum central pressure (mb) of Danielle (2010) on the left and the WRF simulated tracks (right) from 06 UTC 24 August to 06 UTC 30 August. The shaded region in the left panel represents variations among ensembles.

Figure 32 shows the minimum central pressure (left) and track of Hurricane Danielle (right) from 06 UTC 24 August to 06 UTC 30 August. In the simulations, Danielle starts with a minimum central pressure ~978 mb and intensifies to ~940 mb around 00 UTC 28 August. The system then quickly dissipates as it makes a sharp turn to the northeast and becomes an extratropical system by the end of the simulation. The CTRL (blue line), DSTIN (magenta line), and DRAD (red line) show comparable minimum

pressures to the observation (black line). DRAD shows an early intensification and quicker dissipation compared to that of the CTRL and DSTIN. DSTIN shows a higher minimum pressure than both CTRL and DRAD. The track of Danielle in DRAD is further westward after its sharp turn at 03 UTC 28 August, possibly due to the amplification of the mid-level ridge mentioned previously (Figure 29), whereas the DSTIN and CTRL show similar tracks, closer to the observation.

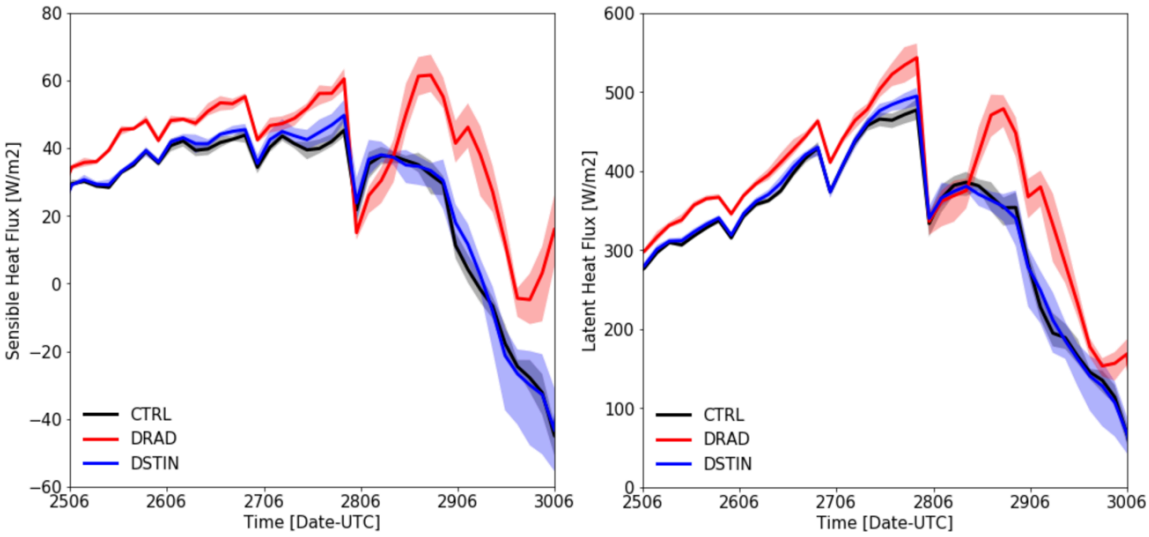

Figure 33: Surface sensible heat flux (W m^{-2}, left) and latent heat flux (W m^{-2}, right) between 06 UTC 25 August and 06 UTC 30 August within 360 km from the center of Danielle.

Figure 33 shows the surface sensible (left) and latent heat (right) fluxes within 360 km from the center of Danielle. The latent heat flux is the dominant source of energy supply to Danielle. Both sensible and latent heat fluxes decrease sharply as Danielle turn northward at 03 UTC 28 August and moves northeastward after 00 UTC 29 August. DRAD shows increases in the low-level wind speed and decreases in the low-level

temperature, which increases the evaporation and upward low-level moisture heat flux and increases the energy supply to the development of Danielle. In general, DRAD shows increases in the surface fluxes throughout the duration of Danielle (as compared to CTRL or DSTIN), providing favorable conditions for its intensification.

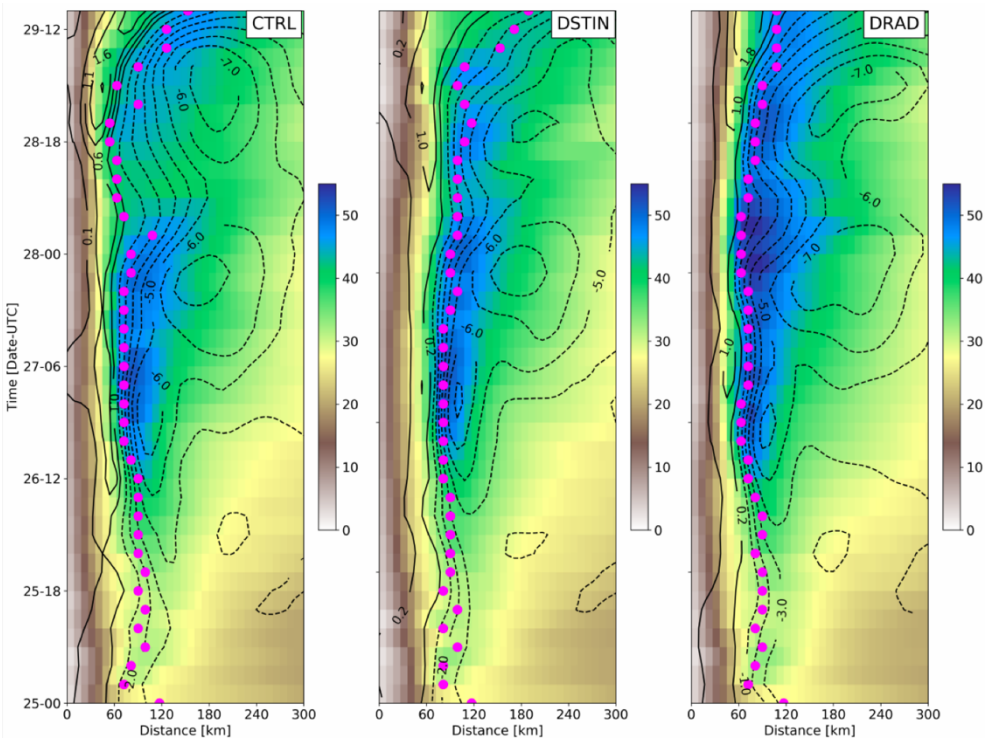

Figure 34: Hovmöller diagram of the azimuthally averaged tangential (color shaded, m s^{-1}) and radial (contours, m s^{-1}) velocities at 1 km from 00 UTC 25 August to 15 UTC 29 August. The magenta dots are the maximum 10 m wind speed locations, corresponding to the size of TCs.

Figure 34 shows the Hovmöller diagram of tangential and radial velocities of Danielle at 1 km, i.e., around the top of the boundary layer. All cases show larger radial and tangential velocities from 12 UTC 26 August to 00 UTC 28 August, indicating the intensification of Hurricane Danielle during this time period. The maximum tangential

velocity reaches ~55 m s^{-1} in DRAD, relatively higher than that of CTRL and DSTIN (~50 m s^{-1}) around 00 UTC 28 August, corresponding to relative lower minimum pressure in DRAD (Figure 32). The time period between 06 UTC 27 and 00 UTC 28 August will be analyzed to investigate dust impacts on the intensification and mature stages of Danielle.

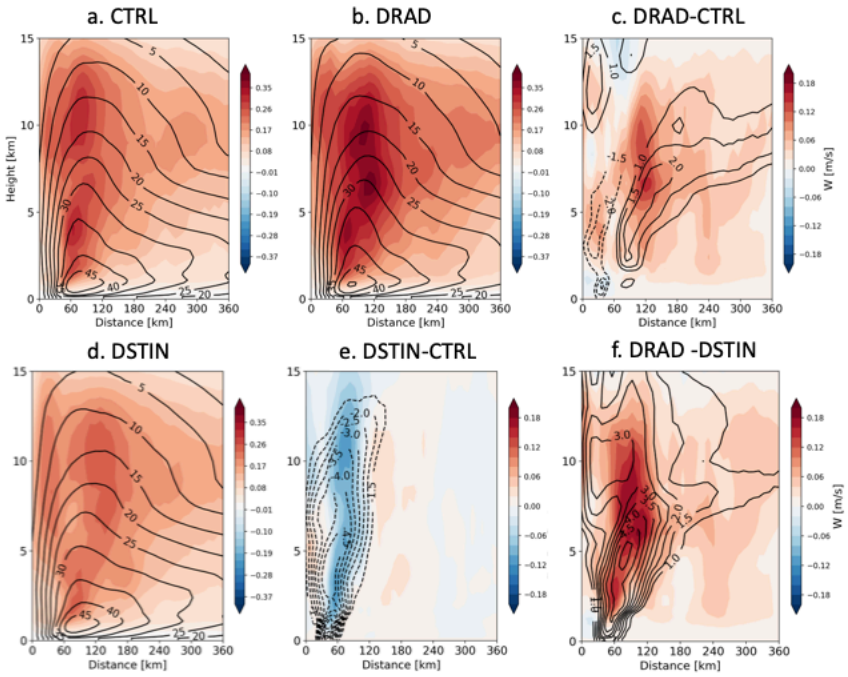

Figure 35: The azimuthally-averaged vertical and tangential velocities (m s^{-1}) from 06 UTC 27 to 00 UTC 28 August for CTRL (a), DRAD (b), DSTIN (d), differences between DRAD and CTRL (c), DSTIN and CTRL (e), and DRAD and DSTIN (f).

Figure 35 shows the azimuthally averaged vertical velocity (color shaded) overlaid with tangential velocity (contours) between 06 UTC 27 and 00 UTC 28 August. The maximum vertical velocity is located between 60 km to 100 km from the eye. DRAD obtains the highest vertical and tangential velocities (0.4 m s^{-1}, 50 m s^{-1}, respectively) among the three scenarios. The difference between DRAD and DSTIN (Figure 35f)

isolates the impact of the dust radiative effect and shows ~0.20 m s^{-1} increase in vertical velocity and ~4.5 m s^{-1} increase in tangential velocity between 30 to 120 km, indicating DRAD has increases in the angular momentum near the eyewall region and possibly enhances the TC intensity. Additionally, the difference in velocity shows a secondary peak ~0.05 m s^{-1} around 200 km from the center of Danielle, possibly owing to the enhanced rainband. The difference between DSTIN and CTRL (Figure 35e) shows both decreases of tangential and vertical velocities in DSTIN (-4.5 m s^{-1} and -0.15 m s^{-1}, respectively) around 60 km from the eye, indicating that dust as INPs possibly increases the size of Danielle and decreases the wind speed due to application of conservation of angular momentum (e.g., see magenta dots in Figure 34). This also explains the up to 10 mb higher minimum central pressure in DSTIN (Figure 32). Figure 35c shows a combination of DRAD and DSTIN effects on vertical velocity and tangential wind, depicting a competing effect between the decrease of vertical velocity in DSTIN and an enhanced vertical velocity in DRAD near the center of Danielle. The overall effect of dust shows an increase in the vertical velocity away from the eye and a second peak of vertical velocity near the rainband region.

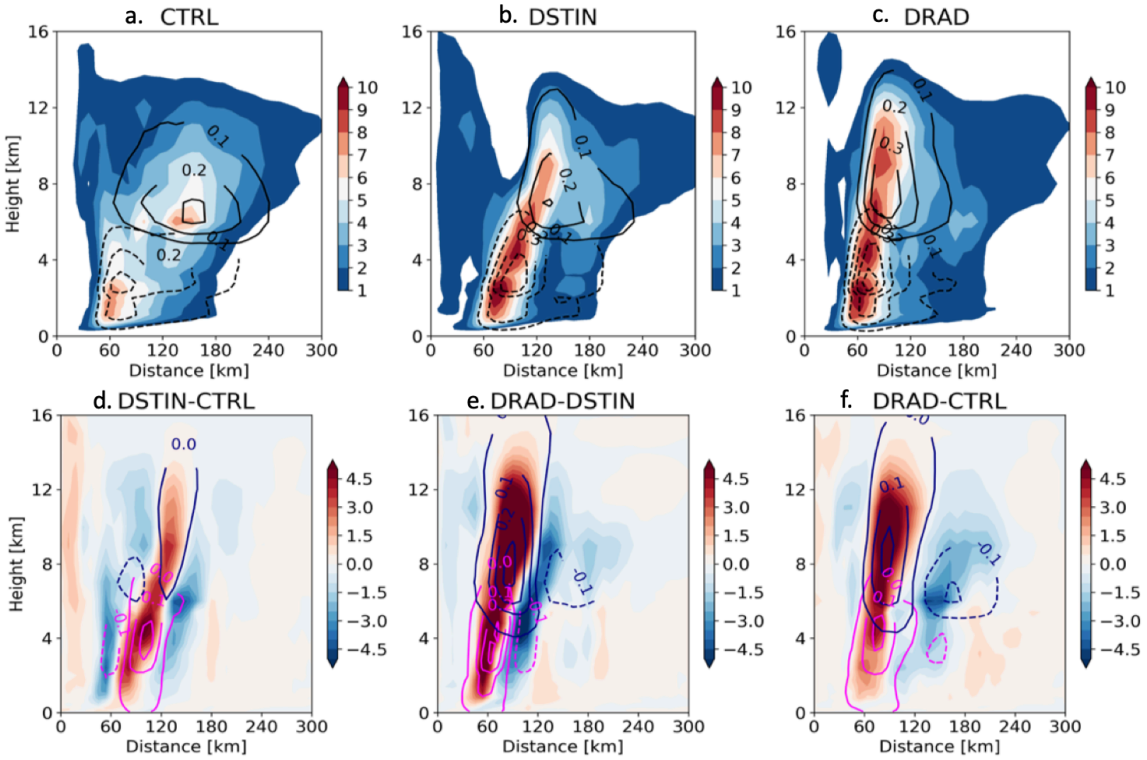

Figure 36: Azimuthally averaged diabatic heating (color shaded, K hr^{-1}), liquid water path (dashed contours, kg m^{-2}), and ice water path (solid contours, kg m^{-2}) from CTRL (a), DSTIN (b), DRAD (c), and difference among DRAD, DSTIN, and CTRL from 06 UTC 27 August to 00 UTC 28 August. Magenta (black) contours in the bottom row represent liquid (ice) water paths.

The azimuthally averaged liquid water path (LWP, dashed contours) and ice water path (IWP, solid contours) show the maxima of LWP and IWP are located near at 3 km and 7 km, respectively (Figure 36, a-c). Both DSTIN and DRAD show higher values of LWP, IWP (contours) and associated diabatic heating than that of CTRL, indicating that dust acting as INP invigorates the convective activities and releases more latent heating (color shaded). The microphysical effect of dust suppresses (enhances) the diabatic heating at 60 km (away from 60 km) (Figure 36d), whereas the radiative effect of dust enhances the diabatic heating rate at around 60 km (Figure 36e), both corresponding to

the vertical velocity change. The combined effects show the increasing of LWP and IWP near the eyewall region, indicating the dominant role of the dust radiative effect. The additional latent heat release likely supports the early intensification of Danielle in DRAD (Figure 32). However, for DSTIN, the enlarged TC size offsets the effect of additional latent release from dust as INP, resulting in relatively higher minimum pressure.

Overall, the dust as INP increases the size of Danielle and suppresses its maximum intensity. The dust radiative effect enhances surface sensible/latent heat fluxes, as well as increases the latent heat release near the eyewall region, thus enhancing the TC intensity. However, due to the relatively small differences in minimum pressure (did not pass the 95% Paired Student T-test), we can only indicate that the radiative effect (microphysical effect) of dust enhances (suppresses) the development of Danielle. The radiative effect of dust dominants the overall impacts on the mature stage TC.

3.3.3 Hurricane Earl

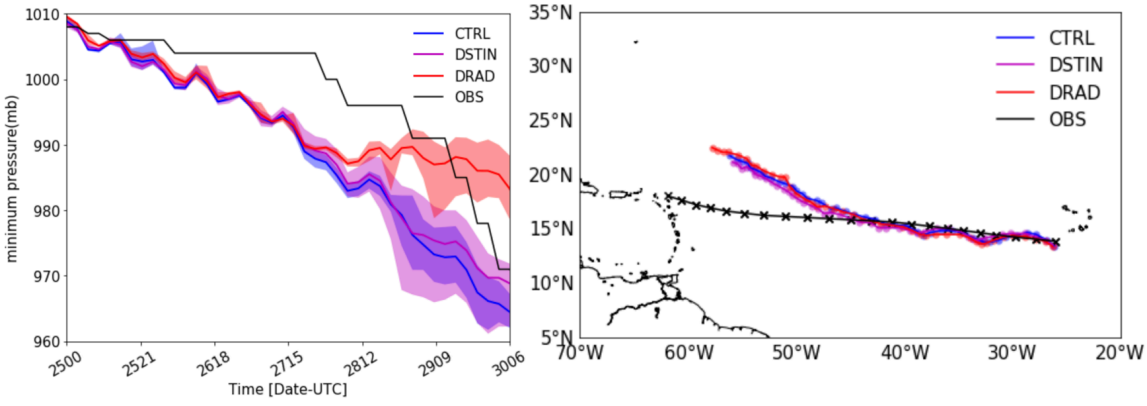

Figure 37: Minimum central pressure (mb) of Earl (2010) on the left and the WRF simulated tracks (right) from 00 UTC 25 August to 06 UTC 30 August. The shaded region in the left panel represents variations among ensemble members.

Figure 37 shows the minimum central pressure and track of Hurricane Earl between 00 UTC 25 August and 06 UTC 30 August. Earl starts ~1010 mb and decreases to ~990 mb at 05 UTC 27 August. Earl continues intensifying and obtains a minimum central pressure between 985-965 mb. All three scenarios show comparable minimum pressures until 15 UTC 27 August, where DRAD shows significantly higher minimum central pressure than the others. The 95% Paired Student T-test shows significant variation (p-value <0.05) between DRAD and CTRL in the minimum central pressure after 18 UTC 27 August. In addition, the radiative effect of dust steers Hurricane Earl on a more northward track at later stages, possibly due to the amplification of mid-level ridge in the mid-Atlantic Ocean (e.g., Figure 29).

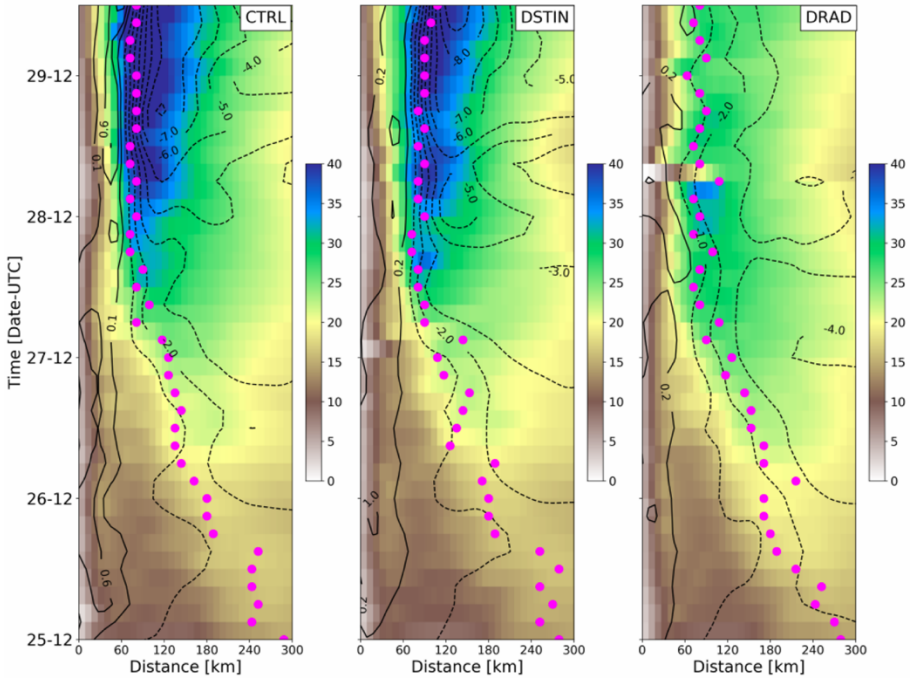

Figure 38: Hovmöller diagram of the azimuthally averaged tangential (color shaded, m s^{-1}) and radial (contours, m s^{-1}) velocities in Earl at 1 km from 12 UTC 25 August to 00

UTC 30 August. The magenta dots are the maximum 10 m wind speed locations, corresponding to the size of TCs.

Both radial and tangential velocities increase as Earl continue intensifying until 06 UTC 30 August (Figure 38). The magnitude for both velocities are similar until the 12 UTC 28 August. The maximum tangential and radial velocities are 8 m s^{-1} and more than 40 m s^{-1} in CTRL, 9 m s^{-1} and more than 40 m s^{-1} in DSTIN, and 4 m s^{-1} and ~30 m s^{-1} in DRAD. The variation in velocities further indicates the difference of intensity between DRAD and other scenarios. Moreover, the size of Earl (magenta dots) decreases as the system intensifies, whereas DSTIN and CTRL reach a relatively stable size by 00 UTC 28 August. The period between 06 UTC 29 August and 00 UTC 30 August, representing the intensification of Earl after the intensity deviation of DRAD, will be analyzed in the following section.

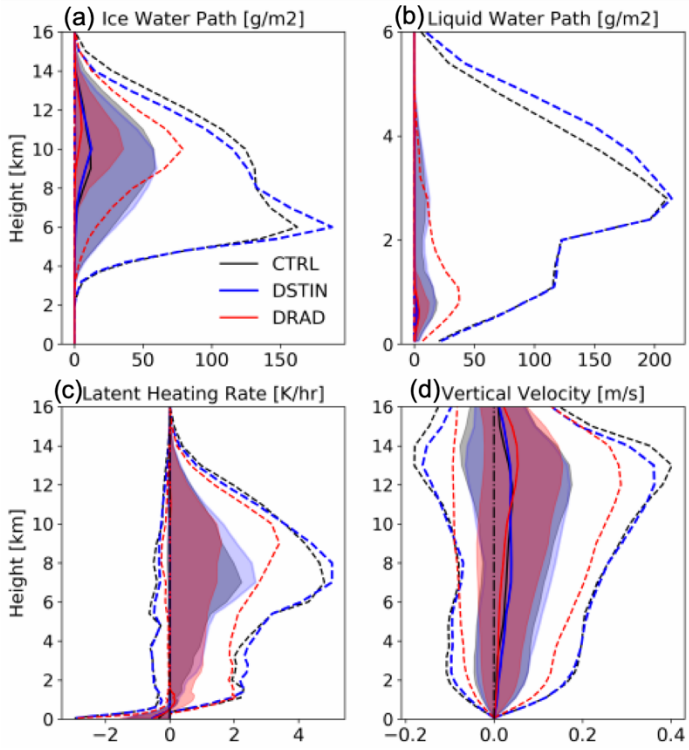

Figure 39: Contoured Frequency by Altitude Diagram of IWP (a, g m^{-2}), LWP (b, g m^{-2}), diabatic heating rate (c, K hr^{-1}), and vertical velocity (d, m s^{-1}) within 360 km from the center of Earl from 06 UTC 29 August to 00 UTC 30 August. The different shapes represent 50% (solid lines), 10% and 90% (dashed lines), and 25% and 75% (shaded regions), respectively.

To investigate the change in diabatic heating rate during the intensification of Earl, we used CFADs to show the vertical distribution of IWP, LWP, diabatic heating rate, and vertical velocity from 06 UTC 29 August to 00 UTC 30 August (Figure 39). The maximum IWP for all scenarios is located at around 10 km. DRAD shows a significantly lower IWP mean value compared to that of CTRL and DSTIN (Figure 39a). In addition, the IWP vertical distribution is similar between CTRL and DSTIN, except slightly higher IWP at the 90th percentile (dashed lines) near 6 km in DSTIN, indicating relatively efficient mixed-phase microphysical processes with dust serving as INPs. For LWP, the maximum

values for the 75th percentile (shaded region) are located near 1 km for all scenarios (Figure 39b). In addition, DSTIN and CTRL show a double maxima of LWP that is found at 1 km and 3 km, respectively, indicating possibly deeper clouds than that of DRAD. Both magnitudes of the 90th percentile (dashed lines) of LWP in DSTIN and CTRL are significantly higher than that of DRAD. The lower magnitudes of LWP and IWP in DRAD result in a lower latent heating rate compared to DSTIN and CTRL (Figure 39c; dashed and shaded region). Interestingly, DRAD also shows a higher altitude of maximum latent heating rate (at 10 km) than that of DSTIN and CTRL (at around 6 km), possibly owing to the increase of temperature and decrease of RH at the mid-level that suppresses ice formation at 6 km. Consequently, the mean values of vertical velocity (solid lines) shows a higher altitude in the DRAD than that of DSTIN and CTRL (Figure 39d). However, the magnitude of latent heating rate and vertical velocity in DRAD are both significantly lower than that of CTRL and DSTIN.

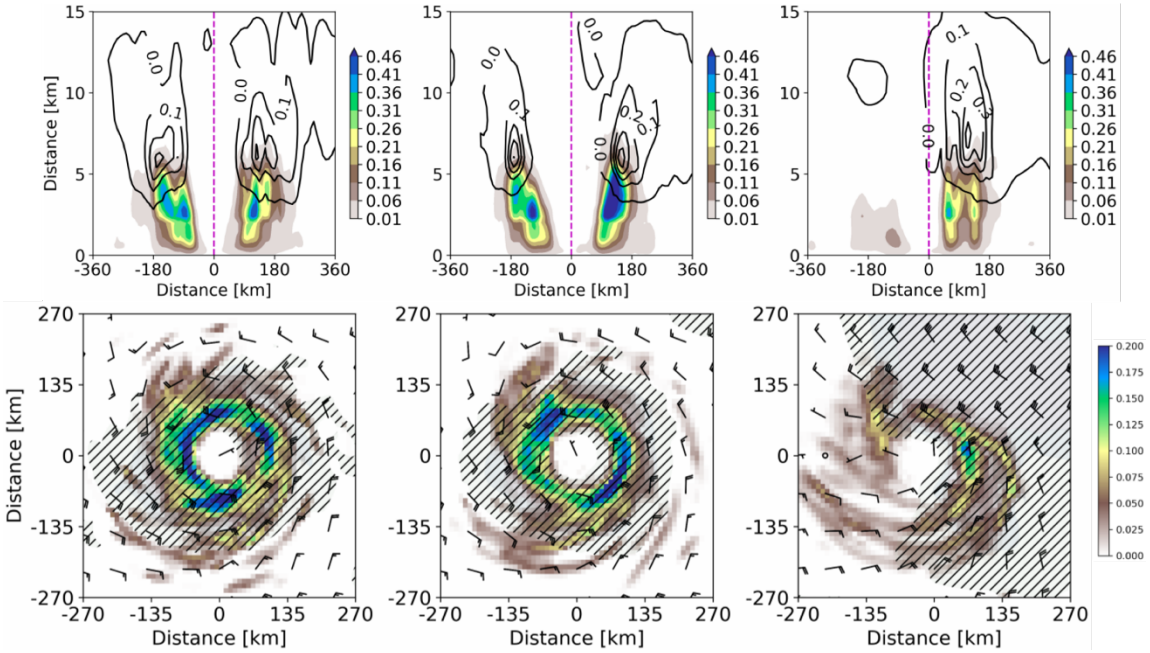

Figure 40: East-west cross section of LWP (color shaded, kg m^{-2}) and IWP (contours, kg m^{-2}) at the top row. The magenta dashed line at the top row represents the center of Earl. A plan view of cloud mixing ratio (g kg^{-1}) at 1 km and vertical wind shear (200–850 mb; half barb = 5 m s^{-1}; full barb = 10 m s^{-1}) at the bottom row. The shaded region at the bottom row represents the vertical wind shear greater than 20 m s^{-1}. Three scenarios are CTRL (left), DSTIN (middle), and DRAD (left). All values are time-averaged between 06 UTC 29 August and 00 UTC 30 August.

The east-west cross section of Earl provides information regarding the vertical and asymmetric structure of Earl during the intensification stage (Figure 40, top row). Both DSTIN and CTRL shows greater LWP values between 60 and 180 km from the center of Earl below 5 km height, whereas only one side of the eyewall appears in relatively lower, but comparable values to DSTIN and CTRL in the DRAD below 5 km height, indicating a highly asymmetric structure in DRAD. In addition, the IWP (Figure 40, contours, top row) shows a larger magnitude, i.e., 0.4 kg m^{-2} for both DRAD and DSTIN, than that of CTRL (0.2 kg m^{-2}), similar to the Danielle case (Figure 36), indicating invigoration of

mixed-phase microphysical processes owing to dust serving as INPs. From a plan view (Figure 40, bottom row), the eye structure is apparent in both DSTIN and CTRL, indicating a highly organized vortex structure. On the other hand, the region of relatively high cloud mixing ratio are only present on the eastern quadrant in DRAD. This is possibly due to the intense environmental vertical wind shear on the eastern side of Earl in DRAD (shaded region), compared to the symmetrically distributed storm-induced vertical wind shear in CTRL and DSTIN.

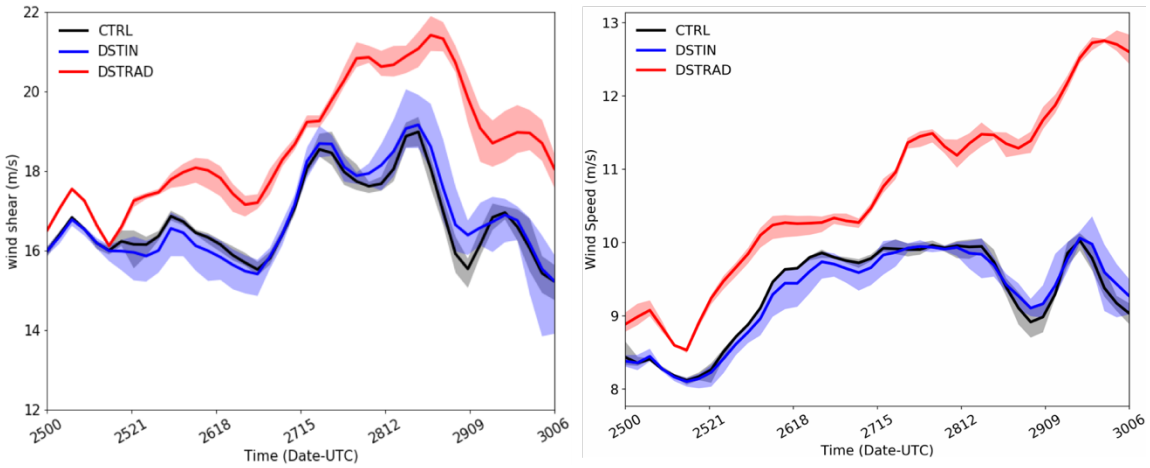

Figure 41: Vertical wind shear (m s^{-1}) between 200 and 850 mb of Hurricane Earl (left) and 850 mb wind (m s^{-1}) from 315 km to 990 km from the center of Earl.

The vertical wind shear between 200 and 850 mb (Figure 41, left) shows that the DRAD case obtains an up to 4 m s^{-1} greater vertical wind shear than that of DSTIN and CTRL. The difference in vertical wind shear is caused by the enhanced low-level wind in DRAD (Figure 41, right). This increased low-level wind suppresses the development of Earl and creates a highly-tilted and shallow vortex (e.g., Figure 40). In addition, both

surface sensible and latent heat fluxes increase as Earl continues intensifying throughout the simulation for all scenarios (Figure 42). DRAD depicts a greater magnitude of both fluxes until 12 UTC 28 August, indicating a thermodynamical favorable condition for the intensification of Earl. The variation of surface heat fluxes after 12 UTC 28 August is possibly due to the lower surface wind speed due to the relatively lower intensity of Earl in DRAD, resultant in hindered surface evaporation.

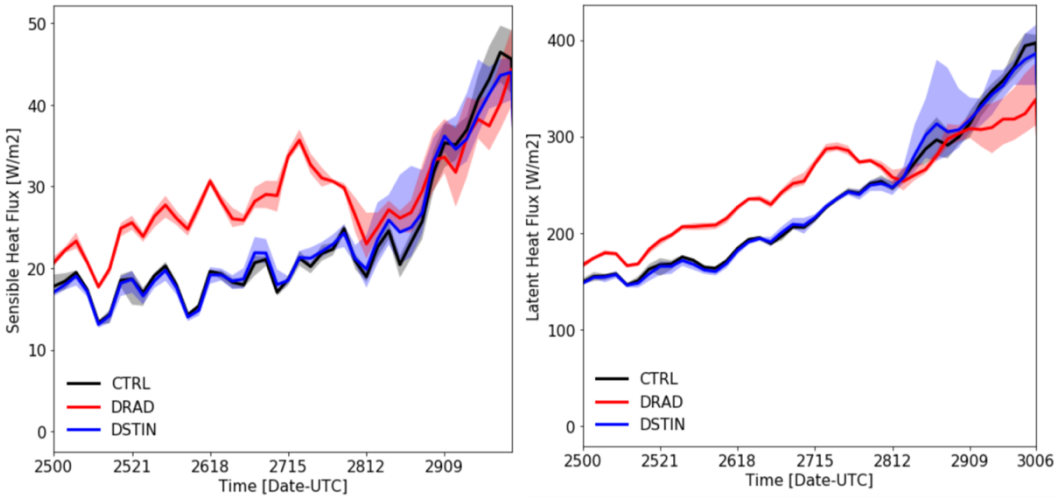

Figure 42: Sensible (left) and latent heat fluxes (right, both in W m^{-2}) from 00 UTC 25 August to 06 UTC 30 August within 360 km from center of Earl.

Overall, both PI and sensible/latent heat fluxes show supportive conditions for Earl's development in DRAD until 12 UTC on 28 August, resulting in comparable minimum pressure. After 12 UTC 28 August, the increased low-level wind (and resultant vertical wind shear) and decreased surface wind as well as latent heat flux, however, suppresses the further intensification of Earl in DRAD.

4. CONCLUSIONS

This dissertation investigated the impacts of natural and anthropogenic aerosols on Atlantic TCs by combining observational analyses and numerical modeling experiments. The objectives of the research were to assess the impacts of Saharan dust on two hurricanes, Danielle and Earl (2010), as well as anthropogenic aerosols on Hurricane Harvey (2017).

The first part of this dissertation evaluated the effect of anthropogenic aerosols during Hurricane Harvey (2017). Harvey produced heavy rainfall of about 555 mm in the Houston urban area during 25-27 August. Combined measurements and numerical model simulations were analyzed to show fundamentally altered cloud microphysical and thermodynamic processes of Hurricane Harvey by anthropogenic aerosols. Ground- and satellite-based lightning and ground-based radar reflectivity measurements were analyzed, showing unusually intense lightning (over 0.23 million strikes) and high radar reflectivity in the Houston region during 26-27 August. The observations revealed heavy precipitation in the proximity of Houston industrial areas, and these hotspots exhibited a remarkable geographic similarity to a decadal climatological maximum of lightning flash density across Southeast Texas (Orville et al. 2001). The effects of anthropogenic aerosols on precipitation and lightning during Harvey was investigated using a CR-WRF model. Two scenarios, a clean (C-case) and a polluted case (P-case), were considered to realistically represent the concentration, emission, and distribution of natural and anthropogenic aerosols over the model domain. Aerosols in both cases consisted of anthropogenic

aerosols and SSAs and was realistically prescribed according to MODIS AOD spatial distribution. The ensemble simulations spanned from 25 to 28 August, covering the most intense precipitation periods in the Houston region. The simulations showed that anthropogenic aerosols increased precipitation and lightning in Houston by a factor of 2-3, unraveling the dominant factor of regulating the energetics and flooding during this extreme weather event.

The second part of this dissertation investigated the effect of Saharan dust during two Atlantic Hurricanes Earl and Danielle (2010). The CR-WRF model was updated to include both microphysical and radiative effects of dust. The dust as INPs, according to (DeMott et al. 2010; Phillips et al. 2008), was implemented into a two-moment microphysics scheme (Li et al. 2008) (DSTIN). The dust radiative effect, based on Hess et al. (1998), was included in the Goddard Shortwave Scheme according to Fan et al. (2008) (DRAD). Three sets of sensitivity experiments were conducted, i.e., CTRL, DSTIN, and DRAD. The simulation covered the intensification of Danielle and Earl, as well as the decay of Danielle, from 06 UTC 24 August to 06 UTC 30 August. The model simulations revealed that the radiative effect of dust significantly decreases low-level temperature and mid-level moisture. Specifically, DRAD decreased the low-level temperature gradient near the West African continent, suppressed thermal wind balance, and weakened the African Easterly Jet. The changes in the temperature field perturbed the large-scale circulation, favoring a stronger mid-level ridge in the DRAD scenario which altered the tracks of Hurricanes Danielle and Earl. On the other hand, DSTIN had little impact on dynamical fields, such as vertical wind shear and the large-scale environmental flow. Furthermore,

analyses of Danielle and Earl showed a significantly suppressed Earl in DRAD, possibly because of the highly asymmetric and shallow vortex due to the large environmental wind shear, as well as a significantly lower surface sensible and latent heat flux, during the intensification of Earl, resulting in significantly higher minimum pressures in DRAD compared to CTRL and DSTIN (e.g., Figure 37). Dust served as INPs enhanced the formation of ice hydrometeors and the increased diabatic heating rate above the freezing level in both DSTIN and DRAD. DSTIN slightly suppressed the intensity of Danielle owing an enlarged size of the TC, but did not significantly perturb the intensity of Earl.

These findings are in agreement with Tao et al. (2018), Shi et al. (2014), and Huang et al. (2019) in that the radiative effect of dust overwhelmed the indirect effect. Moreover, our findings also showed the lack of sensitivity on the tracks of both hurricanes to the dust indirect effect, comparable to findings from Nowottnick et al. (2018). However, we did see that the radiative effect of dust suppressed the genesis of Earl (2010) and favored the intensification of Danielle (2010), indicating different impacts of dust at various stages of hurricanes in agreement with the findings of Pan et al. (2018).

The aerosol effects on tropical cyclones were investigated in this dissertation. Another major effect of aerosols are changes in SST due to the decrease of incoming solar radiation. Atmosphere-ocean coupled simulations are needed for future research of aerosols, especially dust, impacts on Atlantic TCs. In addition, we acknowledge that this dissertation only investigated three Atlantic TCs. More case studies are needed to exclude the case by case factor on the effects of aerosols on Atlantic TCs. To investigate and isolate

the environmental factors as well as aerosol-induced variations, idealized TC simulations will be needed.

REFERENCES

Albrecht, B. A., 1989: Aerosols, Cloud Microphysics, and Fractional Cloudiness. *Science*, **245,** 1227-1230.

Banzon, V., T. M. Smith, T. M. Chin, C. Liu, and W. Hankins, 2016: A long-term record of blended satellite and in situ sea-surface temperature for climate monitoring, modeling and environmental studies. *Earth Syst. Sci. Data*, **8,** 165-176.

Braun, S. A., 2010: Reevaluating the Role of the Saharan Air Layer in Atlantic Tropical Cyclogenesis and Evolution. *Monthly Weather Review*, **138,** 2007-2037.

Bretl, S., P. Reutter, C. C. Raible, S. Ferrachat, C. S. Poberaj, L. E. Revell, and U. Lohmann, 2015: The influence of absorbed solar radiation by Saharan dust on hurricane genesis. *J Geophys Res-Atmos*, **120,** 1902-1917.

Carlson, T. N., and J. M. Prospero, 1972: The large-scale movement of Saharan air outbreaks over the northern equatorial Atlantic. *Journal of applied meteorology*, **11,** 283-297.

Carlson, T. N., and S. G. Benjamin, 1980: Radiative Heating Rates for Saharan Dust. *J Atmos Sci*, **37,** 193-213.

Carrio, G. G., and W. R. Cotton, 2011: Investigations of aerosol impacts on hurricanes: virtual seeding flights. *Atmos. Chem. Phys.*, **11,** 2557-2567.

Carslaw, K. S., and Coauthors, 2013: Large contribution of natural aerosols to uncertainty in indirect forcing. *Nature*, **503,** 67-+.

Chen, D., Z. Q. Liu, C. Davis, and Y. Gu, 2017: Dust radiative effects on atmospheric thermodynamics and tropical cyclogenesis over the Atlantic Ocean using WRF-Chem coupled with an AOD data assimilation system. *Atmos Chem Phys*, **17,** 7917-7939.

Chen, S. H., S. H. Wang, and M. Waylonis, 2010: Modification of Saharan air layer and environmental shear over the eastern Atlantic Ocean by dust-radiation effects. *J Geophys Res-Atmos*, **115,** 22.

Chen, S. H., and Coauthors, 2015: Modeling the effects of dust-radiative forcing on the movement of Hurricane Helene (2006). *Q J Roy Meteor Soc*, **141,** 2563-2570.

d'Almeida, G. A., 1986: A Model for Saharan Dust Transport. *Journal of Climate and Applied Meteorology*, **25,** 903-916.

DeMott, P. J., and Coauthors, 2003: Measurements of the concentration and composition of nuclei for cirrus formation. *P Natl Acad Sci USA*, **100,** 14655-14660.

DeMott, P. J., and Coauthors, 2010: Predicting global atmospheric ice nuclei distributions and their impacts on climate. *P Natl Acad Sci USA*, **107,** 11217-11222.

Dunion, J. P., and C. S. Velden, 2004: The impact of the Saharan air layer on Atlantic tropical cyclone activity. *B Am Meteorol Soc*, **85,** 353-+.

Emanuel, K., 2005: Increasing destructiveness of tropical cyclones over the past 30 years. *Nature*, **436,** 686-688.

Emanuel, K., 2017: Assessing the present and future probability of Hurricane Harvey's rainfall. *Proc Natl Acad Sci U S A*, **114,** 12681-12684.

Evan, A. T., G. R. Foltz, D. X. Zhang, and D. J. Vimont, 2011: Influence of African dust on ocean-atmosphere variability in the tropical Atlantic. *Nat Geosci*, **4,** 762-765.

Evan, A. T., J. Dunion, J. A. Foley, A. K. Heidinger, and C. S. Velden, 2006: New evidence for a relationship between Atlantic tropical cyclone activity and African dust outbreaks. *Geophys Res Lett*, **33**.

Evan, A. T., and Coauthors, 2008: Ocean temperature forcing by aerosols across the Atlantic tropical cyclone development region. *Geochem Geophy Geosy*, **9**.

Fan, J., Y. Wang, D. Rosenfeld, and X. Liu, 2016: Review of Aerosol–Cloud Interactions: Mechanisms, Significance, and Challenges. *J Atmos Sci*, **73,** 4221-4252.

Fan, J., R. Zhang, G. Li, J. Nielsen-Gammon, and Z. Li, 2005: Simulations of fine particulate matter (PM2.5) in Houston, Texas. *Journal of Geophysical Research: Atmospheres*, **110**.

Fan, J., D. Rosenfeld, Y. Yang, C. Zhao, L. R. Leung, and Z. Li, 2015: Substantial contribution of anthropogenic air pollution to catastrophic floods in Southwest China. *Geophys Res Lett*, **42,** 6066-6075.

Fan, J., L. R. Leung, D. Rosenfeld, Q. Chen, Z. Li, J. Zhang, and H. Yan, 2013: Microphysical effects determine macrophysical response for aerosol impacts on deep convective clouds. *Proceedings of the National Academy of Sciences*, **110,** E4581-E4590.

Fan, J., and Coauthors, 2018: Substantial convection and precipitation enhancements by ultrafine aerosol particles. *Science*, **359,** 411-418.

Fan, J. W., R. Y. Zhang, W. K. Tao, and K. I. Mohr, 2008: Effects of aerosol optical properties on deep convective clouds and radiative forcing. *J Geophys Res-Atmos*, **113**.

Goldenberg, S. B., C. W. Landsea, A. M. Mestas-Nuñez, and W. M. Gray, 2001: The Recent Increase in Atlantic Hurricane Activity: Causes and Implications. *Science*, **293,** 474-479.

Gray, W. M., 1998: The formation of tropical cyclones. *Meteorology and Atmospheric Physics*, **67,** 37-69.

Hansen, J., M. Sato, and R. Ruedy, 1997: Radiative forcing and climate response. *J Geophys Res-Atmos*, **102,** 6831-6864.

Hazra, A., P. Mukhopadhyay, S. Taraphdar, J. P. Chen, and W. R. Cotton, 2013: Impact of aerosols on tropical cyclones: An investigation using convection-permitting model simulation. *Journal of Geophysical Research: Atmospheres*, **118,** 7157-7168.

Herbener, S. R., S. C. van den Heever, G. G. Carrio, S. M. Saleeby, and W. R. Cotton, 2014: Aerosol Indirect Effects on Idealized Tropical Cyclone Dynamics. *Journal of the Atmospheric Sciences*, **71,** 2040-2055.

Hess, M., P. Koepke, and I. Schult, 1998: Optical properties of aerosols and clouds: The software package OPAC. *B Am Meteorol Soc*, **79,** 831-844.

Hong, S.-Y., Y. Noh, and J. Dudhia, 2006: A New Vertical Diffusion Package with an Explicit Treatment of Entrainment Processes. *Mon Weather Rev*, **134,** 2318-2341.

Hu, Z. Y., and Coauthors, 2019: Modeling the contributions of Northern Hemisphere dust sources to dust outflow from East Asia. *Atmos. Environ.*, **202,** 234-243.

Huang, C.-C., and Coauthors, 2019: Impacts of Dust–Radiation versus Dust–Cloud Interactions on the Development of a Modeled Mesoscale Convective System over North Africa. *Mon Weather Rev*, **147,** 3301-3326.

Huang, X., Y. Song, C. Zhao, X. Cai, H. Zhang, and T. Zhu, 2015: Direct Radiative Effect by Multicomponent Aerosol over China. *J Climate*, **28,** 3472-3495.

Huneeus, N., and Coauthors, 2011: Global dust model intercomparison in AeroCom phase I. *Atmos Chem Phys*, **11,** 7781-7816.

Iacono, M. J., J. S. Delamere, E. J. Mlawer, M. W. Shephard, S. A. Clough, and W. D. Collins, 2008: Radiative forcing by long-lived greenhouse gases: Calculations with the AER radiative transfer models. *J Geophys Res-Atmos*, **113**.

IPCC, 2013: *Climate Change 2013: The Physical Science Basis. Contribution of Working Group I to the Fifth Assessment Report of the Intergovernmental Panel on Climate Change.* Cambridge University Press, 1535 pp.

Isono, K., M. Komabayasi, and A. Ono, 1959: Volcanoes as a Source of Atmospheric Ice Nuclei. *Nature*, **183,** 317-318.

Kain, J. S., 2004: The Kain–Fritsch Convective Parameterization: An Update. *J Appl Meteorol*, **43,** 170-181.

Kaufman, Y. J., I. Koren, L. A. Remer, D. Tanre, P. Ginoux, and S. Fan, 2005: Dust transport and deposition observed from the Terra-Moderate Resolution Imaging Spectroradiometer (MODIS) spacecraft over the Atlantic ocean. *J Geophys Res-Atmos*, **110**.

Khain, A., B. Lynn, and J. Dudhia, 2010: Aerosol Effects on Intensity of Landfalling Hurricanes as Seen from Simulations with the WRF Model with Spectral Bin Microphysics. *J Atmos Sci*, **67,** 365-384.

Khain, A., B. Lynn, and J. Shpund, 2016: High resolution WRF simulations of Hurricane Irene: Sensitivity to aerosols and choice of microphysical schemes. *Atmos Res*, **167,** 129-145.

Knutson, T. R., and Coauthors, 2010: Tropical cyclones and climate change. *Nature Geoscience*, **3,** 157.

Koch, D., and A. D. Del Genio, 2010: Black carbon semi-direct effects on cloud cover: review and synthesis. *Atmos Chem Phys*, **10,** 7685-7696.

Krall, G. M., and W. R. Cottom, 2012: Potential indirect effects of aerosol on tropical cyclone intensity: convective fluxes and cold-pool activity. *Atmos. Chem. Phys. Discuss.*, **2012,** 351-385.

Lau, K. M., and K. M. Kim, 2007a: How nature foiled the 2006 hurricane forecasts. *Eos, Transactions American Geophysical Union*, **88,** 105-107.

——, 2007b: Cooling of the Atlantic by Saharan dust. *Geophys Res Lett*, **34**.

Levy, M. E., and Coauthors, 2013: Measurements of submicron aerosols in Houston, Texas during the 2009 SHARP field campaign. *Journal of Geophysical Research: Atmospheres*, **118,** 10,518-510,534.

Li, G., Y. Wang, K.-H. Lee, Y. Diao, and R. Zhang, 2009: Impacts of aerosols on the development and precipitation of a mesoscale squall line. *Journal of Geophysical Research*, **114**.

Li, G. H., Y. Wang, and R. Y. Zhang, 2008: Implementation of a two-moment bulk microphysics scheme to the WRF model to investigate aerosol-cloud interaction. *J Geophys Res-Atmos*, **113**.

Lynn, B. H., and Coauthors, 2016: The Sensitivity of Hurricane Irene to Aerosols and Ocean Coupling: Simulations with WRF Spectral Bin Microphysics. *J Atmos Sci*, **73,** 467-486.

Ma, P.-L., K. Zhang, J. J. Shi, T. Matsui, and A. Arking, 2012: Direct Radiative Effect of Mineral Dust on the Development of African Easterly Waves in Late Summer, 2003–07. *Journal of Applied Meteorology and Climatology*, **51,** 2090-2104.

Milbrandt, J. A., and M. K. Yau, 2005: A multimoment bulk microphysics parameterization. Part I: Analysis of the role of the spectral shape parameter. *J Atmos Sci*, **62,** 3051-3064.

Nowottnick, E. P., and Coauthors, 2018: Dust Impacts on the 2012 Hurricane Nadine Track during the NASA HS3 Field Campaign. *Journal of the Atmospheric Sciences*, **75,** 2473-2489.

Orville, R. E., and Coauthors, 2001: Enhancement of cloud-to-ground lightning over Houston, Texas. *Geophys Res Lett*, **28,** 2597-2600.

Pan, B., and Coauthors, 2018: Impacts of Saharan Dust on Atlantic Regional Climate and Implications for Tropical Cyclones. *J Climate*, **31,** 7621-7644.

Patricola, C. M., and M. F. Wehner, 2018: Anthropogenic influences on major tropical cyclone events. *Nature*, **563,** 339-346.

Peng, J. F., and Coauthors, 2016: Markedly enhanced absorption and direct radiative forcing of black carbon under polluted urban environments. *Proceedings of the National Academy of Sciences of the United States of America*, **113,** 4266-4271.

Phillips, V. T. J., P. J. DeMott, and C. Andronache, 2008: An Empirical Parameterization of Heterogeneous Ice Nucleation for Multiple Chemical Species of Aerosol. *Journal of the Atmospheric Sciences*, **65,** 2757-2783.

Qu, Y., B. Chen, J. Ming, B. H. Lynn, and M.-J. Yang, 2017: Aerosol Impacts on the Structure, Intensity, and Precipitation of the Landfalling Typhoon Saomai (2006). *Journal of Geophysical Research: Atmospheres*, **122,** 11,825-811,842.

Reale, O., K. M. Lau, A. da Silva, and T. Matsui, 2014: Impact of assimilated and interactive aerosol on tropical cyclogenesis. *Geophys Res Lett*, **41,** 3282-3288.

Rosenfeld, D., W. L. Woodley, A. Khain, W. R. Cotton, G. Carrio, I. Ginis, and J. H. Golden, 2012: Aerosol Effects on Microstructure and Intensity of Tropical Cyclones. *B Am Meteorol Soc*, **93,** 987-1001.

Rosenfeld, D., and Coauthors, 2008: Flood or Drought: How Do Aerosols Affect Precipitation? *Science*, **321,** 1309-1313.

Schepanski, K., I. Tegen, and A. Macke, 2009: Saharan dust transport and deposition towards the tropical northern Atlantic. *Atmos Chem Phys*, **9,** 1173-1189.

Seigel, R. B., S. C. van den Heever, and S. M. Saleeby, 2013: Mineral dust indirect effects and cloud radiative feedbacks of a simulated idealized nocturnal squall line. *Atmos. Chem. Phys.*, **13,** 4467-4485.

Shao, Y. P., and Coauthors, 2011: Dust cycle: An emerging core theme in Earth system science. *Aeolian Res*, **2,** 181-204.

Shi, J. J., and Coauthors, 2014: Implementation of an aerosol–cloud-microphysics–radiation coupling into the NASA unified WRF: Simulation results for the 6–7 August 2006 AMMA special observing period. *Q J Roy Meteor Soc*, **140,** 2158-2175.

Shpund, J., A. Khain, and D. Rosenfeld, 2019: Effects of Sea Spray on the Dynamics and Microphysics of an Idealized Tropical Cyclone. *J Atmos Sci*, **76,** 2213-2234.

Strong, J. D. O., G. A. Vecchi, and P. Ginoux, 2018: The Climatological Effect of Saharan Dust on Global Tropical Cyclones in a Fully Coupled GCM. *J Geophys Res-Atmos*, **123,** 5538-5559.

Sun, D. L., W. K. M. Lau, M. Kafatos, Z. Boybeyi, G. Leptoukh, C. W. Yang, and R. X. Yang, 2009: Numerical Simulations of the Impacts of the Saharan Air Layer on Atlantic Tropical Cyclone Development. *J Climate*, **22,** 6230-6250.

Tang, B., and K. Emanuel, 2012: A Ventilation Index for Tropical Cyclones. *B Am Meteorol Soc*, **93,** 1901-1912.

Tao, W.-K., and Coauthors, 2011: The impact of microphysical schemes on hurricane intensity and track. *Asia-Pacific Journal of Atmospheric Sciences*, **47,** 1-16.

Tao, Z., S. A. Braun, J. J. Shi, M. Chin, D. Kim, T. Matsui, and C. D. Peters-Lidard, 2018: Microphysics and Radiation Effect of Dust on Saharan Air Layer: An HS3 Case Study. *Monthly Weather Review*, **146,** 1813-1835.

Thompson, G., and T. Eidhammer, 2014: A Study of Aerosol Impacts on Clouds and Precipitation Development in a Large Winter Cyclone. *J Atmos Sci*, **71,** 3636-3658.

Trenberth, K., 2005: Uncertainty in Hurricanes and Global Warming. *Science*, **308,** 1753-1754.

Trenberth, K. E., L. Cheng, P. Jacobs, Y. Zhang, and J. Fasullo, 2018: Hurricane Harvey Links to Ocean Heat Content and Climate Change Adaptation. *Earth's Future*, **6,** 730-744.

Twomey, S., 1974: Pollution and the planetary albedo. *Atmospheric Environment (1967)*, **8,** 1251-1256.

van Oldenborgh, G. J., and Coauthors, 2017: Attribution of extreme rainfall from Hurricane Harvey, August 2017. *Environmental Research Letters*, **12**.

Wang, C., S. Dong, A. T. Evan, G. R. Foltz, and S.-K. Lee, 2012: Multidecadal Covariability of North Atlantic Sea Surface Temperature, African Dust, Sahel Rainfall, and Atlantic Hurricanes. *J Climate*, **25,** 5404-5415.

Wang, S. Y. S., L. Zhao, J.-H. Yoon, P. Klotzbach, and R. R. Gillies, 2018: Quantitative attribution of climate effects on Hurricane Harvey's extreme rainfall in Texas. *Environmental Research Letters*, **13**.

Wang, Y., A. Khalizov, M. Levy, and R. Zhang, 2013: New Directions: Light absorbing aerosols and their atmospheric impacts. *Atmos Environ*, **81,** 713-715.

Wang, Y., K.-H. Lee, Y. Lin, M. Levy, and R. Zhang, 2014: Distinct effects of anthropogenic aerosols on tropical cyclones. *Nature Clim. Change*, **4,** 368-373.

Wang, Y., Q. Wan, W. Meng, F. Liao, H. Tan, and R. Zhang, 2011: Long-term impacts of aerosols on precipitation and lightning over the Pearl River Delta megacity area in China. *Atmospheric Chemistry and Physics*, **11,** 12421-12436.

Webster, P. J., G. J. Holland, J. A. Curry, and H.-R. Chang, 2005: Changes in Tropical Cyclone Number, Duration, and Intensity in a Warming Environment. *Science*, **309,** 1844-1846.

Williams, E. R., R. Zhang, and J. Rydock, 1991: Mixed-Phase Microphysics and Cloud Electrification. *Journal of the Atmospheric Sciences*, **48,** 2195-2203.

Willoughby, H. E., D. P. Jorgensen, R. A. Black, and S. L. Rosenthal, 1985: Project Stormfury - a Scientific Chronicle 1962-1983. *B Am Meteorol Soc*, **66,** 505-514.

Yu, H., and Coauthors, 2019: Estimates of African Dust Deposition Along the Trans-Atlantic Transit Using the Decade-long Record of Aerosol Measurements from CALIOP, MODIS, MISR, and IASI. *Journal of Geophysical Research: Atmospheres*.

Zhang, H., G. M. McFarquhar, S. M. Saleeby, and W. R. Cotton, 2007: Impacts of Saharan dust as CCN on the evolution of an idealized tropical cyclone. *Geophysical Research Letters*, **34**.

Zhang, H. N., G. M. McFarquhar, W. R. Cotton, and Y. Deng, 2009: Direct and indirect impacts of Saharan dust acting as cloud condensation nuclei on tropical cyclone eyewall development. *Geophysical Research Letters*, **36**.

Zhang, R., and Coauthors, 2015: Formation of urban fine particulate matter. *Chem Rev*, **115,** 3803-3855.

Zhang, R. Y., A. Khalizov, L. Wang, M. Hu, and W. Xu, 2012: Nucleation and Growth of Nanoparticles in the Atmosphere. *Chemical Reviews*, **112,** 1957-2011.

Zhang, W., G. Villarini, G. A. Vecchi, and J. A. Smith, 2018: Urbanization exacerbated the rainfall and flooding caused by hurricane Harvey in Houston. *Nature*, **563,** 384-+.

Zhang, X., and Coauthors, 2016: Representing Multiple Scales in the Hurricane Weather Research and Forecasting Modeling System: Design of Multiple Sets of Movable Multilevel Nesting and the Basin-Scale HWRF Forecast Application. *Weather and Forecasting*, **31,** 2019-2034.

Zhao, C., Y. Lin, F. Wu, Y. Wang, Z. Li, D. Rosenfeld, and Y. Wang, 2018: Enlarging Rainfall Area of Tropical Cyclones by Atmospheric Aerosols. *Geophys Res Lett*, **45,** 8604-8611.